

# The effect of symmetry breaking on the dynamics near a structurally stable heteroclinic cycle between equilibria and a periodic orbit

Vivien Kirk , Department of Mathematics, University of Auckland,  
 Private Bag 92019, Auckland, New Zealand

Alastair M. Rucklidge , Department of Applied Mathematics, University of Leeds,  
 Leeds LS2 9JT, UK  
 (November 28, 2018)

The effect of small forced symmetry breaking on the dynamics near a structurally stable heteroclinic cycle connecting two equilibria and a periodic orbit is investigated. This type of system is known to exhibit complicated, possibly chaotic dynamics including irregular switching of sign of various phase space variables, but details of the mechanisms underlying the complicated dynamics have not previously been investigated. We identify global bifurcations that induce the onset of chaotic dynamics and switching near a heteroclinic cycle of this type, and by construction and analysis of approximate return maps, locate the global bifurcations in parameter space. We find there is a threshold in the size of certain symmetry-breaking terms below which there can be no persistent switching. Our results are illustrated by a numerical example.

## 1 Introduction

It is well-established that the presence of symmetries in dynamical systems can result in the existence of heteroclinic cycles that are structurally stable with respect to symmetric perturbations [1, 2]. By *heteroclinic cycle* we mean a collection of flow invariant sets  $\{\xi_1, \dots, \xi_n\}$  of some system of ordinary differential equations together with a set of heteroclinic connections  $\{\gamma_1(t), \dots, \gamma_n(t)\}$ , where  $\gamma_j(t) \rightarrow \xi_j$  as  $t \rightarrow -\infty$  and  $\gamma_j(t) \rightarrow \xi_{j+1}$  as  $t \rightarrow +\infty$ , and where  $\xi_{n+1} \equiv \xi_1$ . In many studies, all the  $\xi_i$  are equilibria, but in this

paper we explicitly consider the case that one of the  $\xi_i$  is a periodic orbit. The connections  $\gamma_i$  may be isolated, or there may be a continuum of connections from  $\xi_i$  to  $\xi_{i+1}$  for one or more  $i$ .

There is a large literature on structurally stable heteroclinic cycles (SSHC), including work establishing conditions for the existence and asymptotic stability of heteroclinic cycles [3–5], examination of the dynamics near heteroclinic cycles and networks of heteroclinic cycles [6–9], and unfolding of bifurcations of heteroclinic cycles [10–12]. SHCC arise naturally in mathematical models of physical systems with symmetry or near-symmetry [13–15]. In these models, the physical system is idealised as having perfect symmetry, leading to the existence of invariant subspaces in the model and thus to the robustness of heteroclinic cycles with respect to symmetric perturbations. It is natural to ask how much of the dynamics observed in symmetric models persists under non-symmetric perturbations. Some effects of small symmetry-breaking have been documented [16–19], and aspects of the related question of how much of the dynamics persists under the inclusion of small noise have also been considered [20, 21], but details are likely to vary greatly between different examples.

Our interest in the particular set-up explored in this paper is motivated by [19], which makes the observation that the addition of small symmetry-breaking terms to a system containing a heteroclinic cycle connecting two equilibria and a periodic orbit (as well as symmetric copies of the cycle) results in seemingly chaotic dynamics, with orbits passing near the various equilibria in the system repeatedly but in an irregular pattern, as illustrated in figure 1. A main point of [19] was to show that repeated switching of orbits in this manner could arise in a simple four-dimensional, nearly symmetric model, but the specific mechanisms underlying the complicated dynamics were not explored in detail.

In this paper, we examine a generalisation of the situation from [19], focusing on the structure and origin of chaotic dynamics in the system and on how switching dynamics is induced. Here and elsewhere in the paper, *switching* refers to the itinerary that an orbit follows under the dynamics. Specifically, in the fully symmetric version of our system there are four symmetric copies of the basic heteroclinic cycle. Invariance of various subspaces ensures that an orbit may make repeated passes near only one cycle. Once the symmetries are broken, however, an orbit may *switch*, i.e., make traversals near more than

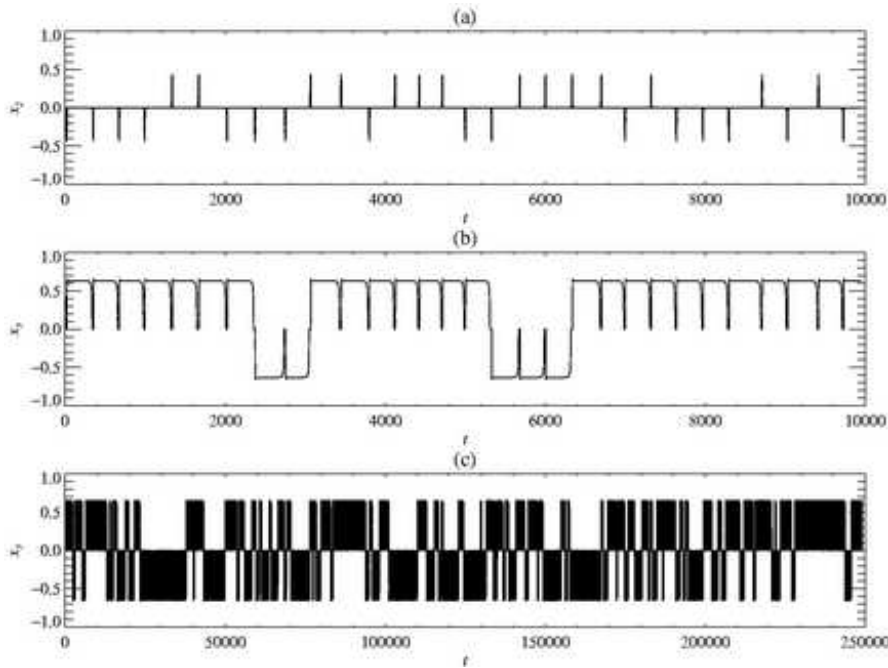


Figure 1. Irregular switching in the time series of a dynamo model studied in [19, figure 1]. Panels (a) and (b) show the evolution of different coordinates of the same trajectory, and panel (c) shows the same coordinate as in (b) over a longer time interval.

one of the original cycles (although, of course, the cycles themselves may not persist when the symmetry is broken).

A main result of this paper is that in the case of small symmetry breaking, switching in one variable occurs when a complicated attractor arising from the presence of transverse homoclinic orbits of a periodic orbit crosses the stable manifold of one of the equilibria in the system; the existence of the transverse homoclinic orbits depends on a broken rotation (or normal form) symmetry, while the proximity of the attractor to the stable manifold of the equilibrium is caused by a broken reflection symmetry. Switching in a second variable results from the interaction between broken reflection symmetry and complicated dynamics associated with a heteroclinic bifurcation between the equilibria. Thus, switching results from the right combination of a global bifurcation and small symmetry breaking.

A second significant result of this paper is the observation that a certain threshold for the size of symmetry breaking exists; below this threshold persistent switching cannot occur. More precisely, the existence of the heteroclinic

cycle requires three separate symmetries to allow structurally stable connections within three invariant subspaces. We control the degree to which the three symmetries are broken by three small parameters,  $\epsilon_1$ ,  $\epsilon_2$  and  $\epsilon_3$ . In particular,  $\epsilon_1$  controls the degree to which the periodic orbit in the cycle deviates from a perfect circle, while  $\epsilon_2$  and  $\epsilon_3$  break reflection symmetries. For fixed small  $\epsilon_2$  and  $\epsilon_3$ , we find that there is a threshold in  $\epsilon_1$  for persistent switching to occur. For sufficiently small  $\epsilon_1$ , there may be a single switch from one part of phase space to another, but it is only for  $\epsilon_1$  beyond this threshold value that the dynamics repeatedly visits different parts of the phase space. We find that it is possible to get sustained switching in one or other or both of the variables associated with the reflection symmetries, and that the threshold values of  $\epsilon_1$  are different for the two variables. The threshold does not go to zero as  $\epsilon_2$  and  $\epsilon_3$  go to zero.

Sustained switching of orbits near heteroclinic cycles and networks has been observed in a number of other settings. Clune and Knobloch [22] describe an example in which there are two symmetrically related copies of a non-asymptotically stable heteroclinic cycle, with nearby orbits making repeated passes near each cycle; no mechanism for the switching is suggested in this paper. Aguiar et al. [8] find switching near a hybrid heteroclinic network formed from transverse heteroclinic connections between equilibria and connections that are robust because of symmetry; switching seems to result from the folding and stretching caused by passage near the transversal heteroclinic connections and by mixing near an equilibrium solution with complex eigenvalues. Kirk et al. [23] have an example of switching near a heteroclinic network that has no transversal connections; the switching is caused entirely by passage near an equilibrium with complex eigenvalues. Postlethwaite and Dawes [9] describe a variant of switching near a heteroclinic network in which each cycle in the network is unstable along a direction transverse to the cycle; orbits visit cycles in the network in a fixed order (being pushed away from each cycle in the transverse direction which also happens to be the contracting direction for the next cycle) but the number of traversals of each cycle before switching to the next cycle can be constant or irregular. Ashwin et al. [24] describe switching associated with a stuck-on heteroclinic cycle between two invariant subspaces; here the switching is a nonlinear mechanism that chooses between the different possibilities in a manner that is well modelled by a ran-

dom process. Switching can also be induced by adding noise to a structurally stable heteroclinic network [21]; noise sensitive switching has been observed by [25, 26]. None of these examples explicitly considers symmetry breaking as a mechanism for switching.

We adopt a standard approach to analysis of the system of interest, i.e., we set up a simple symmetric model in which there exists a heteroclinic cycle connecting two equilibria and a periodic orbit (Section 2), construct a return map that approximates the dynamics near such a cycle, and then add generic symmetry breaking terms to the return map (Section 3). Analysis of the return map is fruitful in cases where partial symmetry is retained, and allows us to prove the existence and asymptotic stability of periodic orbits, quasiperiodic solutions or heteroclinic cycles in various cases (Sections 4.1–4.3). In the completely asymmetric case, the return map is intractable, but we are able to make predictions about the dynamics by assuming there is a generic unfolding of the partially symmetric cases (Section 4.4). The example discussed in Section 5 confirms and illustrates the analysis. Some conclusions are presented in Section 6.

A complicating factor in the analysis presented in this paper is that the unstable manifolds of one pair of equilibria and of the periodic orbit are two-dimensional, and there are continua of heteroclinic connections along some parts of the cycle in the fully symmetric case. Linearising about a single heteroclinic connection is not appropriate, and the usual method of analysis needs to be adapted to keep track of orbits in a neighbourhood of all the connections. Our approach is similar to that taken in [7, 23, 27]. We note that our analysis need not consider the issue of which connection from a continuum is selected by the dynamics (as investigated in, for instance, [7, 24, 28, 29]) since in our case breaking of the symmetries forces a discrete set of transversal connections to be selected from each continuum.

## 2 Description of the problem

We consider a system of ordinary differential equations  $\dot{\mathbf{x}} = \mathbf{f}(\mathbf{x})$  where  $\mathbf{f} : \mathbb{R}^4 \rightarrow \mathbb{R}^4$ , and  $\mathbf{x} = (x_1, y_1, x_2, x_3) \in \mathbb{R}^4$ . It is sometimes convenient to use polar coordinates  $(r_1, \theta_1)$  such that  $z_1 \equiv x_1 + i y_1 \equiv r_1 e^{i\theta_1}$ . Initially, we assume the system is equivariant with respect to the action of a rotation and two

reflections:  $\kappa_i(\mathbf{f}(\mathbf{x})) = \mathbf{f}(\kappa_i(\mathbf{x}))$ ,  $i = 1, 2, 3$ , where

$$\kappa_1: (z_1, x_2, x_3) \rightarrow (z_1 e^{i\phi}, x_2, x_3),$$

$$\kappa_2: (z_1, x_2, x_3) \rightarrow (z_1, -x_2, x_3),$$

$$\kappa_3: (z_1, x_2, x_3) \rightarrow (z_1, x_2, -x_3),$$

with  $0 \leq \phi < 2\pi$ . The presence of these symmetries ensures the existence of some dynamically invariant subspaces. We make the following assumptions about the dynamics in the subspaces, as illustrated in figure 2:

- There exists a hyperbolic periodic orbit  $P$  in the invariant plane  $x_2 = x_3 = 0$ . Within this plane, the periodic orbit is a sink.
- There exist hyperbolic, symmetry-related pairs of equilibria  $\pm E_2$  and  $\pm E_3$  on the invariant lines  $z_1 = 0, x_3 = 0$  and  $z_1 = 0, x_2 = 0$  respectively. Within these lines, the equilibria are sinks.
- Within the invariant subspace  $x_3 = 0$ ,  $P$  is a saddle and  $\pm E_2$  are sinks, and there are two-dimensional manifolds of heteroclinic connections from  $P$  to  $\pm E_2$  (figure 2a).
- Within the invariant subspace  $z_1 = 0$ ,  $\pm E_2$  are saddles and  $\pm E_3$  are sinks, and there are one-dimensional heteroclinic connections from  $\pm E_2$  to  $\pm E_3$ , and from  $-E_2$  to  $\pm E_3$  (figure 2b).
- Within the invariant subspace  $x_2 = 0$ ,  $\pm E_3$  are saddles and  $P$  is a sink, and there are two-dimensional manifolds of heteroclinic connections from  $\pm E_3$  to  $P$  (figure 2c).

In the presence of the rotation symmetry  $\kappa_1$ , the coordinate  $\theta_1$  decouples from the other coordinates, leaving an equivalent three-dimensional system containing a SSHC connecting three saddle-type equilibria. This cycle may be asymptotically stable, depending on the eigenvalues at the three equilibria [4]. The behaviour of trajectories near such a heteroclinic cycle is well understood, with a typical orbit passing near each of the equilibria in a cyclic manner, spending ever increasing periods of time near each equilibrium. The dynamics in the fully symmetric, four-dimensional problem therefore has analogous behaviour: trajectories cycle between two equilibria and a periodic orbit, with the time spent near each equilibrium or the periodic orbit increasing with each subsequent traversal of the cycle [19]. Moving to four dimensions does more

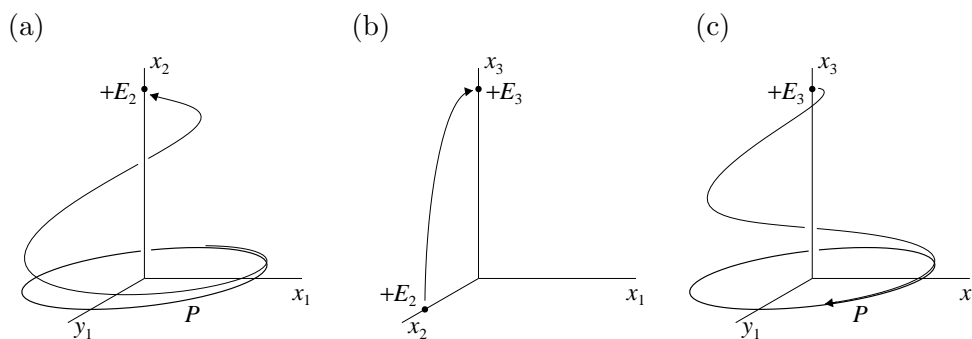


Figure 2. The heteroclinic cycle for the fully symmetric system. (a) One of the connections in the  $x_3 = 0$  subspace, from the periodic orbit  $P$  to the equilibrium point  $+E_2$ ; (b) the single connection in the  $x_1 = y_1 = 0$  subspace, between the equilibria  $+E_2$  and  $+E_3$ ; (c) one of the connections in the  $x_2 = 0$  subspace, from  $+E_3$  to  $P$ .

than just replace one equilibrium by a periodic orbit: it also introduces dynamical features that will be important once symmetry is broken. In particular, as can be seen in figure 2,  $E_2$  and  $E_3$  are saddle-foci in the four-dimensional problem and  $E_3$  has a two-dimensional unstable manifold.

A detailed analysis of the effect on the dynamics of small symmetry breaking is performed in the following sections; here we describe some geometric effects. Since  $\pm E_2$ ,  $\pm E_3$  and  $P$  are assumed to be hyperbolic in the fully symmetric case, they all persist and are hyperbolic when sufficiently small symmetry breaking terms are added. However,  $E_2$  and  $-E_2$  will generically move off the  $x_2$ -axis and will no longer be related to each other by symmetry. Generic symmetry breaking will have an analogous effect on  $E_3$  and  $-E_3$ , and will also break the circular symmetry of the  $P$  and move it off the plane  $x_2 = x_3 = 0$ .

Sufficiently small symmetry breaking will not change the dimensions of the stable and unstable manifolds of  $\pm E_2$ ,  $\pm E_3$  and  $P$  but it will destroy the fixed point subspaces, and the heteroclinic connections that existed in the subspaces will either cease to exist or change their nature. We consider the geometric effect of symmetry breaking on each of the former heteroclinic connections in turn.

A heteroclinic connection from  $E_2$  to  $E_3$  requires the coincidence in  $\mathbb{R}^4$  of a one-dimensional and a two-dimensional manifold; this connection will be destroyed by a generic symmetry-breaking perturbation.

A heteroclinic connection from  $E_3$  to  $P$  occurs when the two-dimensional unstable manifold of  $E_3$  intersects the three-dimensional stable manifold of  $P$ ;

depending on the perturbation, we generically expect to see either transversal intersections between these manifolds (in which case there are at least two robust heteroclinic connections from  $E_3$  to  $P$ ) or no intersections of the manifolds. The special case where the manifolds are tangent can also occur in a codimension-one way. In the case of transversal intersections of manifolds, we might expect to see heteroclinic tangles and the associated complicated dynamics, depending on whether the dynamics elsewhere in the phase space permits reinjection of trajectories into the neighbourhood of the transversal intersections.

A heteroclinic connection from  $P$  to  $E_2$  occurs when the two-dimensional unstable manifold of  $P$  intersects the three-dimensional stable manifold of  $E_2$ . There is a clear analogy with the case of connections from  $E_3$  to  $P$  and the comments about that case apply equally here.

While small symmetry-breaking terms will generically destroy the heteroclinic cycle, there will still be an attractor lying close to the original heteroclinic cycle (Melbourne [16] shows this in a closely related case). As we show below, the form of this attractor (e.g., periodic, quasiperiodic, chaotic) depends on the nature of the symmetry-breaking perturbations included. We note that in the fully symmetric case, invariance of the two subspaces defined by  $x_2 = 0$  and  $x_3 = 0$  respectively means that trajectories are restricted to one quarter of the phase space: each trajectory visits just one quarter of the full attractor. However, once the symmetries are broken, a single trajectory may explore a much larger region of the phase space. We are interested in determining the circumstances under which trajectories exhibit switching, i.e., make passages near two or more quarters of the original heteroclinic attractor.

### 3 Construction of a return map

In this section, we use standard techniques to construct and analyse a return map that approximates the dynamics near the cycle. We define local coordinates and cross-sections near  $\pm E_2$ ,  $\pm E_3$  and  $P$ , then determine local maps valid in a neighbourhood of each of  $\pm E_2$ ,  $\pm E_3$  and  $P$ , and global maps valid in a neighbourhood of each heteroclinic connection. Composing the local and global maps yields the desired return map. Throughout, we use a small parameter  $h$  to control the size of the local neighbourhoods ( $h \ll 1$ ), and small



parameters  $\epsilon_1, \epsilon_2, \epsilon_3$  to control the extent to which the symmetries  $\kappa_1, \kappa_2, \kappa_3$  are broken. Since symmetry breaking will cause the periodic orbit and equilibrium points to move, we assume that  $\epsilon_i \ll h$ , so that the shifted periodic orbit and equilibria stay away from the edges of the local neighbourhoods. With this assumption, we argue below that the dynamics in the local neighbourhoods will be unaffected by the symmetry breaking (to leading order in the  $\epsilon_i$ 's), and all symmetry-breaking effects can be taken into account in the global maps. We freely interchange between the forms of variables  $z_1, (r_1, \theta_1)$  and  $(x_1, y_1)$ , and explicitly label the four positions in the domain and the range of each map whenever there is any possibility of ambiguity.

### 3.1 Local coordinates

Following [4], we distinguish radial, contracting, and expanding directions near the equilibria in the fully symmetric case. Specifically, writing  $\mathcal{P}_1 = \{(z_1, x_2, x_3) : x_3 = 0\}$ ,  $\mathcal{P}_2 = \{(z_1, x_2, x_3) : z_1 = 0\}$ ,  $\mathcal{P}_3 = \{(z_1, x_2, x_3) : x_2 = 0\}$ , with  $\mathcal{P}_0 \equiv \mathcal{P}_3$ , then the radial eigenvalues at  $\pm E_j$  ( $j = 2, 3$ ) are the eigenvalues of the linearised vector field at  $\pm E_j$  (i.e., eigenvalues of  $(d\mathbf{f})_{\pm E_j}$ ) restricted to  $\mathcal{P}_j \cap \mathcal{P}_{j-1}$ . The contracting eigenvalues are the remaining eigenvalues of  $(d\mathbf{f})_{\pm E_j}$  in  $\mathcal{P}_{j-1}$ , and the expanding eigenvalues are the remaining eigenvalues in  $\mathcal{P}_j$ . The radial direction is then the span of the eigenvectors corresponding to the radial eigenvalues, and similarly for the contracting and expanding directions. Near  $P$  we define the radial direction to be the direction of  $\mathcal{P}_1 \cap \mathcal{P}_3$  (i.e., the plane  $x_2 = x_3 = 0$ ), the contracting direction is parallel to the  $x_3$ -axis, and the expanding direction is parallel to the  $x_2$ -axis. These definitions are consistent with those in [4] (where the cycle connects equilibria) but are adapted for the case where there is a periodic orbit in the heteroclinic cycle.

We adopt local coordinates near each of  $P, \pm E_2$ , and  $\pm E_3$ , that make the linearised dynamics as simple as possible. Near  $E_2$  in the fully symmetric case, we define  $\xi_2 = x_2 - \bar{x}_2$ , where  $\bar{x}_2$  is the value of  $x_2$  at  $E_2$ , and then use local coordinates  $(z_1, \xi_2, x_3)$ ;  $z_1, \xi_2$  and  $x_3$  correspond to the contracting, radial and expanding directions, respectively. Under symmetry breaking,  $E_2$  moves in proportion to the magnitude of the symmetry breaking, and the local coordinates are measured from the new position of the equilibrium point. The

eigenvalues and eigenvectors change similarly, but since the eigenvalues are generically distinct and non-zero, small symmetry-breaking will not change the nature of the local structure and we can use the slightly altered eigenvectors to define a slightly altered local coordinate system. We continue to identify radial, contracting and expanding directions once weak symmetry breaking is introduced, in the obvious way, and retain the notation  $(z_1, \xi_2, x_3)$ , for the altered coordinates, although  $z_1$  and  $x_3$  may no longer coincide with the corresponding global coordinates.

A similar construction is used near  $-E_2$  except that  $\xi_2 = -x_2 + \bar{x}_2$ , where  $\bar{x}_2$  is the value of  $x_2$  at  $-E_2$ . The point of defining  $\xi_2$  in this way is that positive values of  $\xi_2$  near  $E_2$  are mapped under the reflection  $\kappa_2$  to positive values of  $\xi_2$  near  $-E_2$ , and this simplifies the maps we derive below. An analogous procedure is used to define local coordinates near  $\pm E_3$ .

To construct local coordinates near  $P$ , we select a cross-section transverse to  $P$ , say  $\theta_1 = 0$ . Near  $P$ , the flow induces a map from that section to itself, with  $P$  corresponding to a fixed point of the map. We define  $\xi_1 = r_1 - \bar{r}_1$ , where  $\bar{r}_1$  is the value of  $r_1$  at the fixed point;  $\xi_1$  is the analogue in the map to the radial coordinate for the flow near  $P$ . The remaining local coordinates on the cross-section are defined by restricting the expanding and contracting directions at  $P$ , as defined above, to the cross-section. Local coordinates can be extended to a neighbourhood of the whole of  $P$  (not just the intersection of  $P$  with  $\theta_1 = 0$ ) in the fully symmetric case by applying equivariance under  $\kappa_1$ . Finally, small symmetry-breaking perturbations will not change the local structure near  $P$ , and we can extend to slightly altered local coordinates  $(\xi_1, \theta_1, x_2, x_3)$  in a neighbourhood of  $P$  so long as we remember that symmetry-breaking terms may have a different effect at each value of  $\theta_1$ , so for instance,  $z_1 = \bar{r}_1 e^{i\theta_1}$  where  $\bar{r}_1 \equiv r_1(\theta_1)$  is a function of  $\theta_1$ . Note that the global polar coordinates  $(r_1, \theta_1)$  are well-defined near  $P$  even in the presence of small symmetry breaking since  $P$  is far from the origin.

### 3.2 Cross-sections

Cross-sections in  $\mathbb{R}^4$  are defined in terms of local coordinates as follows:

$$\begin{aligned} H_1^{\text{in}} &= \{(\xi_1, \theta_1, x_2, x_3) : |\xi_1| \leq h, 0 \leq \theta_1 < 2\pi, |x_2| \leq h, |x_3| = h\}, \\ H_1^{\text{out}} &= \{(\xi_1, \theta_1, x_2, x_3) : |\xi_1| \leq h, 0 \leq \theta_1 < 2\pi, |x_2| = h, |x_3| \leq h\}, \\ H_2^{\text{in}} &= \{(z_1, \xi_2, x_3) : |z_1| = h, |\xi_2| \leq h, |x_3| \leq h\}, \\ H_2^{\text{out}} &= \{(z_1, \xi_2, x_3) : |z_1| \leq h, |\xi_2| \leq h, |x_3| = h\}, \\ H_3^{\text{in}} &= \{(z_1, x_2, \xi_3) : |z_1| \leq h, |x_2| = h, |\xi_3| \leq h\}, \\ H_3^{\text{out}} &= \{(z_1, x_2, \xi_3) : |z_1| = h, |x_2| \leq h, |\xi_3| \leq h\}. \end{aligned}$$

The cross-sections  $H_2^{\text{in}}$  and  $H_2^{\text{out}}$  (resp.  $H_3^{\text{in}}$  and  $H_3^{\text{out}}$ ) work equally well near  $\pm E_2$  (resp.  $\pm E_3$ ) so long as the local coordinate  $\xi_2$  (resp.  $\xi_3$ ) is interpreted correctly, as described above.

We also define a Poincaré section for the periodic orbit  $P$ :

$$H_1^P = \{(\xi_1, \theta_1, x_2, x_3) : |\xi_1| \leq h, \theta_1 = 0, |x_2| \leq h, |x_3| \leq h\}.$$

Trajectories visiting  $P$  first cross  $H_1^{\text{in}}$ , may then cross  $H_1^P$  several times, and eventually leave the neighbourhood of  $P$  on crossing  $H_1^{\text{out}}$ .

### 3.3 Local maps

Within a neighbourhood of each of  $\pm E_2$ ,  $\pm E_3$  and  $P$ , so long as certain non-resonance conditions on the eigenvalues are satisfied, the dynamics can be linearised using the Hartman–Grobman theorem [31]. In the fully symmetric case, the dynamics near  $P$  can be approximated by:

$$\dot{\xi}_1 = -2\xi, \quad \dot{\theta}_1 = 1, \quad \dot{x}_2 = e_1 x_2, \quad \dot{x}_3 = -c_1 x_3,$$

where  $e_1$  and  $c_1$  are positive constants. Here we have, without loss of generality, assumed that the radial eigenvalue (i.e., the coefficient of  $\xi_1$  in the  $\dot{\xi}_1$  equation) is  $-2$ , and that the angular speed (i.e., the constant on the right hand side of the  $\dot{\theta}_1$  equation) is 1. Solving these equations, we find that a trajectory that

starts on  $H_1^{\text{in}}$  at time  $t = 0$  crosses  $H_1^{\text{out}}$  at

$$\begin{aligned}\xi_1(T_1) &= \xi_1(0) \left| \frac{x_2(0)}{h} \right|^{\gamma_1}, & \theta_1(T_1) &= \theta_1(0) + T_1, \\ x_2(T_1) &= h \operatorname{sgn}(x_2(0)), & x_3(T_1) &= h \operatorname{sgn}(x_3(0)) \left| \frac{x_2(0)}{h} \right|^{\delta_1},\end{aligned}$$

where  $\operatorname{sgn}(x) = +1$  if  $x > 0$ ,  $\operatorname{sgn}(x) = -1$  if  $x < 0$ , and  $\operatorname{sgn}(0) = 0$ , where  $\delta_1 = c_1/e_1$ ,  $\gamma_1 = 2/e_1$ , and where

$$T_1 = -\frac{1}{e_1} \ln \left| \frac{x_2(0)}{h} \right|.$$

Thus the local map  $\phi_1 : H_1^{\text{in}} \rightarrow H_1^{\text{out}}$  is given by:

$$\phi_1(\xi_1, \theta_1, x_2, x_3) = \left( \xi_1 \left| \frac{x_2}{h} \right|^{\gamma_1}, \theta_1 - \frac{1}{e_1} \ln \left| \frac{x_2}{h} \right|, h \operatorname{sgn}(x_2), h \operatorname{sgn}(x_3) \left| \frac{x_2}{h} \right|^{\delta_1} \right), \quad (1)$$

where the initial value of  $x_3$  satisfies  $|x_3| = h$ .

The argument that symmetry-breaking makes no difference to the local map just derived goes as follows. The transition from  $H_1^{\text{in}} \rightarrow H_1^{\text{out}}$  can be considered in three parts. First, the trajectory travels from  $H_1^{\text{in}} \rightarrow H_1^P$  in less than one circuit around  $P$ . The trajectory does not very get close to  $P$  in this time, having started at least a distance  $h$  from it. Since the  $\epsilon_i$ 's, which control the symmetry breaking, are assumed to be much smaller than  $h$ , the fully symmetric flow yields an adequate approximation of the true flow. Second, the trajectory makes  $n_1$  circuits around the periodic orbit from  $H_1^P$  to  $H_1^P$ , where  $n_1$  is a non-negative integer no greater than  $T_1/2\pi$ . These circuits are governed by the linearised Poincaré map and its Floquet multipliers:  $e^{-4\pi}$ ,  $e^{2\pi e_1}$  and  $e^{-2\pi c_1}$  in the radial, expanding and contracting directions, respectively, where, to leading order in the  $\epsilon_i$ 's, the period of  $P$  is  $2\pi$ . The number  $n_1$  of iterates is unchanged by the weakly broken symmetry, and so, to leading order, this part of the map is unchanged. Third, the trajectory travels from  $H_1^P \rightarrow H_1^{\text{out}}$  in less than one circuit around  $P$  and again is not too close to  $P$ , so the fully symmetric flow yields an adequate approximate of the true flow. Composing the three parts described here yields (1), to leading order.

Similarly, local maps  $\phi_2 : H_2^{\text{in}} \rightarrow H_2^{\text{out}}$  and  $\phi_3 : H_3^{\text{in}} \rightarrow H_3^{\text{out}}$  can be calcu-

lated:

$$\phi_2(r_1 = h, \theta_1, \xi_2, x_3) = \left( h \left| \frac{x_3}{h} \right|^{\delta_2}, \theta_1 - \frac{1}{e_2} \ln \left| \frac{x_3}{h} \right|, \xi_2 \left| \frac{x_3}{h} \right|^{\gamma_2}, h \operatorname{sgn}(x_3) \right), \quad (2)$$

and

$$\phi_3(r_1, \theta_1, x_2, \xi_3) = \left( h, \theta_1 - \frac{1}{e_3} \ln \left( \frac{r_1}{h} \right), h \operatorname{sgn}(x_2) \left( \frac{r_1}{h} \right)^{\delta_3}, \xi_3 \left( \frac{r_1}{h} \right)^{\gamma_3} \right), \quad (3)$$

with  $|x_2| = h$ . In these maps,  $c_i$  and  $e_i$  are constants (the absolute values of the real parts of the contracting and expanding eigenvalues at  $E_i$ ),  $\delta_i = c_i/e_i$ , and  $\gamma_i = 2/e_i$ . Without loss of generality, the radial eigenvalue has been set to  $-2$  and the angular speed has been set to 1 in each case.

### 3.4 Global maps

The main idea in constructing global maps between  $P$ ,  $E_2$  and  $E_3$  is to linearise around a known trajectory or family of trajectories. In the fully symmetric case there are structurally stable connections  $P \rightarrow E_2$ ,  $E_2 \rightarrow E_3$  and  $E_3 \rightarrow P$  and the behaviour of trajectories near each connection can be estimated by Taylor expansion. Symmetry-breaking effects are then included by Taylor expansion in powers of the  $\epsilon_i$ . A complicating feature of this construction is that the unstable manifolds of  $P$  and  $E_3$  are two-dimensional.

The global map  $\Psi_{12} : H_1^{\text{out}} \rightarrow H_2^{\text{in}}$  takes orbits from a neighbourhood of  $P$  to a neighbourhood of  $E_2$ . We write

$$\Psi_{12}(\xi_1, \theta_1, x_2 = h, x_3) = (\tilde{r}_1 = h, \tilde{\theta}_1, \tilde{\xi}_2, \tilde{x}_3)$$

and initially do not include any symmetry-breaking effects. The unstable manifold of  $P$  is two-dimensional and, locally, intersects the outgoing cross-section  $H_1^{\text{out}}$  in a one-dimensional set:

$$\mathcal{W}^u(P) \cap H_1^{\text{out}} = \{(\xi_1, \theta_1, x_2, x_3) : \xi_1 = 0, 0 \leq \theta_1 < 2\pi, x_2 = \pm h, x_3 = 0\} \quad (4)$$

The manifold  $\mathcal{W}^u(P)$  has two branches: the *positive* branch intersects  $H_1^{\text{out}}$  with  $x_2 = h$  and the *negative* branch intersects  $H_1^{\text{out}}$  with  $x_2 = -h$ . The positive branch forms a connection from  $P$  to  $E_2$  and is the solution set we

now linearise about, while the negative branch forms the connection from  $P$  to  $-E_2$  and will be discussed later. The positive branch of  $\mathcal{W}^u(P)$  intersects  $H_2^{\text{in}}$  at the one-dimensional set

$$\{(r_1, \theta_1, \xi_2, x_3) : r_1 = h, 0 \leq \theta_1 < 2\pi, \xi_2 = \bar{\xi}_2, x_3 = 0\} \quad (5)$$

where  $\bar{\xi}_2$  is a small constant. As a result of the  $\kappa_1$  rotation symmetry, we find that the heteroclinic orbit corresponding to the choice  $\theta_1$  in (4) has an angular component in  $H_2^{\text{in}}$  of  $\theta_1 + \bar{\theta}_1$  for some constant  $\bar{\theta}_1$ , i.e., the global map acts on the angle as a rigid rotation. Furthermore, trajectories that are near but not on the unstable manifold of  $\mathcal{W}^u(P)$  have  $\tilde{\xi}_2$  and  $\tilde{x}_3$  depending on the initial  $\xi_1$  and  $x_3$  but not on  $\theta_1$ , while  $\tilde{\theta}_1 = \theta_1 + \bar{\theta}_1$  where  $\bar{\theta}_1$  is a function of the initial  $\xi_1$  and  $x_3$ . Equivariance under  $\kappa_3$  ensures that the subspace  $x_3 = 0$  is invariant, that  $\tilde{x}_3$  is an odd function of  $x_3$ , and that  $\bar{\theta}_1$  and  $\tilde{\xi}_2$  are even functions of  $x_3$ . (The  $\kappa_2$  symmetry has no role in determining the form of  $\Psi_{12}$  although it can be used to construct a map from  $P$  to  $-E_2$  once  $\Psi_{12}$  is known.) Writing a Taylor series in the small quantities  $\xi_1$  and  $x_3$  therefore yields

$$\begin{aligned} \tilde{\theta}_1(\xi_1, \theta_1, x_3) &= \theta_1 + \bar{\theta}_1(\xi_1, x_3) = \theta_1 + \bar{\theta}_1(0, 0) + \text{h.o.t.}, \\ \tilde{\xi}_2(\xi_1, x_3) &= \tilde{\xi}_2(0, 0) + \text{h.o.t.}, \\ \tilde{x}_3(\xi_1, x_3) &= \frac{\partial \tilde{x}_3}{\partial x_3}(0, 0) x_3 + \text{h.o.t.}, \end{aligned}$$

where h.o.t. denotes higher order terms. Effectively, so long as  $\bar{\theta}_1$  and  $\tilde{\xi}_2$  are non-zero, they can be replaced by constants, while  $\tilde{x}_3$  depends linearly on  $x_3$ . We write  $A_1 = \frac{\partial \tilde{x}_3}{\partial x_3}(0, 0)$  and  $B_1 = \tilde{\xi}_2(0, 0)$ , and note that  $A_1 > 0$  since the region of phase space with  $x_3 > 0$  is dynamically invariant.

We now consider the effect on these expressions of the inclusion of weak symmetry breaking. First, the symmetry  $x_3 \rightarrow -x_3$  is broken by including terms that are odd in  $x_3$  in the expressions for  $\tilde{\theta}_1$  and  $\tilde{\xi}_2$ , and terms that are even in  $x_3$  in the expression for  $\tilde{x}_3$ . We think of all such terms as being multiplied by an overall factor of  $\epsilon_3$ , which is a real constant that controls the magnitude of the breaking of the  $\kappa_3$  symmetry. Then the lowest order contribution to  $\tilde{\theta}_1$  and  $\tilde{\xi}_2$  will be a term in  $\epsilon_3 x_3$  while  $\tilde{x}_3$  will pick up a term linear in  $\epsilon_3$ . At leading order all the quadratic terms can be dropped, so the only new term is one

linear in  $\epsilon_3$  in the expression for  $\tilde{x}_3$ . Second, breaking the  $\kappa_1$  symmetry will result in a weak dependence of all the coefficients on  $\theta_1$ , with the dependence being periodic in that variable. We introduce the parameter  $\epsilon_1$ , which is a real constant that multiplies all terms that break the  $\kappa_1$  symmetry and that controls the magnitude of the symmetry-breaking terms. For example,  $A_1$  will become  $A_1 + \epsilon_1 f_1(\theta)$ , with the caveat that this term must remain positive, for all  $\theta$  and  $\epsilon_1$ . Third, weakly breaking the symmetry  $x_2 \rightarrow -x_2$  will not affect the form of this map. Of course, the effect of breaking this last symmetry does not completely disappear from the approximate dynamics but, as we will see, enters at leading order in one of the other global maps.

Putting all this together results in a map  $\Psi_{12} : H_1^{\text{out}} \rightarrow H_2^{\text{in}}$ :

$$\begin{aligned} \Psi_{12}(\xi_1, \theta_1, x_2 = h, x_3) &= (\tilde{r}_1 = h, \tilde{\theta}_1 = \theta_1 + \Phi_1, \tilde{\xi}_2 = B_1, \\ \tilde{x}_3 &= A_1 x_3 + \epsilon_3 + \epsilon_1 x_3 f_1(\theta_1) + \epsilon_1 \epsilon_3 g_1(\theta_1)), \end{aligned} \quad (6)$$

where  $\Phi_1, A_1, B_1$  are constants, and  $f_1, g_1$  are  $2\pi$ -periodic functions of  $\theta_1$ . Note that the  $\theta_1$  dependence cannot be treated using Taylor series expansions, as  $\theta_1$  is not a small quantity. We explain below why some quadratic terms ( $\epsilon_1 x_3$  and  $\epsilon_1 \epsilon_3$ ) need to be kept.

In a similar way, a global map from  $P$  to  $-E_2$  can be constructed. This map has precisely the form of the map (6), except that it starts from  $x_2 = -h$ . Due to breaking of the  $\kappa_2$  symmetry, all coefficients in the map will be slightly different but this effect is of higher order than the terms retained, and so the map is unaffected at leading order.

The map  $\Psi_{23} : H_2^{\text{out}} \rightarrow H_3^{\text{in}}$  is calculated in a similar way. In the fully symmetric case, we linearise about the unstable manifold of  $E_2$ , which intersects  $H_2^{\text{out}}$  at  $(z_1 = 0, \xi_2 = 0, x_3 = h)$  and  $H_3^{\text{in}}$  at  $(z_1 = 0, \xi_2 = h, \xi_3 = \bar{\xi}_3)$  where  $\bar{\xi}_3$  is a small constant. For orbits near the unstable manifold of  $E_2$ , the value of  $\xi_2$  at  $H_2^{\text{out}}$  does not influence the final position to leading order and  $z_1$  at  $H_3^{\text{in}}$  depends linearly on the values of  $z_1$  at  $H_2^{\text{out}}$ :  $\tilde{z}_1 = A_2 e^{i\Phi_2} z_1$  for real constants  $A_2 > 0, \Phi_2$ . If the  $\kappa_1$  symmetry is broken, the unstable manifold of  $E_2$  leaves  $H_2^{\text{out}}$  with  $z_1 = 0$  and arrives at  $H_3^{\text{in}}$  with  $z_1 = \tilde{\epsilon}_1$ , where  $\tilde{\epsilon}_1 = \epsilon_1(a_r + ia_i)$  for  $a_r$  and  $a_i$  real constants and  $\epsilon_1$  as defined earlier. Writing the resulting map

in terms of the real and imaginary parts of  $\tilde{z}_1$ :

$$\begin{aligned}\Psi_{23}(r_1, \theta_1, \xi_2, x_3 = h) &= (\tilde{x}_1 = \epsilon_1 a_r + A_2 r_1 \cos(\theta_1 + \Phi_2), \\ \tilde{y}_1 &= \epsilon_1 a_i + A_2 r_1 \sin(\theta_1 + \Phi_2), \\ \tilde{x}_2 &= h, \tilde{\xi}_3 = B_2),\end{aligned}\tag{7}$$

where  $a_r$ ,  $a_i$ ,  $A_2$ ,  $B_2$  and  $\Phi_2$  are all real constants determined by the global flow, and  $A_2 > 0$ . As in  $\Psi_{12}$ , there are  $2\pi$ -periodic functions of  $\theta_1$  in the map, but here the functions are known explicitly because the  $z_1$  variable is small throughout the transition from  $E_2$  to  $E_3$ , and the dynamics of  $z_1$  is well-approximated by a scaled rotation. Similar maps can be obtained for the three connections  $-E_2 \rightarrow E_3$  and  $\pm E_2 \rightarrow -E_3$ ; although the coefficients will be slightly different in each case, to lowest order we obtain the same map for each of the other connections so long as the signs of the  $x_3$  (resp.  $\tilde{x}_2$ ) components are chosen appropriately on the incoming (resp. outgoing) cross-sections (for example, the map from  $-E_2$  to  $-E_3$  will have  $x_3 = -h$  and  $\tilde{x}_2 = -h$ ).

The global map  $\Psi_{31} : H_3^{\text{out}} \rightarrow H_1^{\text{in}}$  is calculated in a similar way:

$$\begin{aligned}\Psi_{31}(r_1 = h, \theta_1, x_2, \xi_3) &= (\tilde{\xi}_1 = B_3, \tilde{\theta}_1 = \theta_1 + \Phi_3, \\ \tilde{x}_2 &= A_3 x_2 + \epsilon_2 + \epsilon_1 x_2 f_3(\theta_1) + \epsilon_1 \epsilon_2 g_3(\theta_1), \\ \tilde{x}_3 &= h),\end{aligned}\tag{8}$$

where  $A_3$ ,  $B_3$  and  $\Phi_3$  are real constants,  $f_3$  and  $g_3$  are  $2\pi$ -periodic functions of  $\theta_1$ , and  $\epsilon_1$  controls the size of the terms that break the  $\kappa_1$  symmetry. The parameter  $\epsilon_2$  introduced in (8) is analogous to  $\epsilon_3$ , and is a real quantity that controls the size of all terms that break the  $\kappa_2$  symmetry. Similarly to the case for  $A_1$  argued above, we take  $A_3 + \epsilon_1 f_3(\theta_1)$  to be positive for all values of  $\epsilon_1$ . A similar map can be defined near the connections from  $-E_3$  to  $P$ , and will, to leading order, be identical to (8) so long as  $\tilde{x}_3 = h$  is replaced by  $\tilde{x}_3 = -h$ .

The effect of each of the global maps defined above is, at leading order, to rotate the angular variable by an order one amount that is independent of other variables, to set the radial variable to a constant, and, in the absence of symmetry-breaking, to scale the variable that measures proximity to the



cycle. Symmetry-breaking effects enter in two ways. First, symmetry breaking destroys the invariant subspaces thus destroying some of the heteroclinic connections that made up the cycle. Second, breaking the  $\kappa_1$  rotation symmetry allows  $\theta_1$  dependence to enter into the maps, most importantly through the variables  $x_3$  in the  $\Psi_{12}$  map and  $x_2$  in the  $\Psi_{31}$  map. It is this  $\theta_1$  dependence that allows the heteroclinic tangencies discussed in Section 2. For our discussion below of the way in which breaking the  $\kappa_1$  symmetry can induce persistent switching in the  $x_3$  and  $x_2$  variables, it is convenient to rewrite the  $x_3$  component of the map  $\Psi_{12}$  as  $\tilde{x}_3 = x_3(A_1 + \epsilon_1 f_1(\theta_1)) + \epsilon_3(1 + \epsilon_1 g_1(\theta_1))$  (and similarly the  $x_2$  component of the map  $\Psi_{31}$ ).

### 3.5 Return maps

Appropriate composition of the local and global maps given above yields a return map that approximates the dynamics near the heteroclinic cycle. As an intermediate step, it is convenient to write down composite maps, each consisting of one local map composed with one global map. Without loss of generality, we rescale constants (such as  $A_1$  and  $\Phi_1$ ) and functions (such as  $f_1$  and  $g_1$ ) by order one amounts (compared with the  $\epsilon_i$ ), to simplify the maps.

Defining  $C_1 \equiv \Psi_{12} \circ \phi_1 : H_1^{\text{in}} \rightarrow H_2^{\text{in}}$ , we have:

$$\begin{aligned} C_1(\xi_1, \theta_1, x_2, x_3 = \pm_3 h) = & \left( \tilde{r}_1 = h, \tilde{\theta}_1 = \theta_1 + \Phi_1 - \frac{1}{e_1} \ln |x_2|, \tilde{\xi}_2 = B_1, \right. \\ & \tilde{x}_3 = \pm_3 A_1 |x_2|^{\delta_1} \pm_3 \epsilon_1 |x_2|^{\delta_1} f_1\left(\theta_1 - \frac{1}{e_1} \ln |x_2|\right) \\ & \left. + \epsilon_3 + \epsilon_1 \epsilon_3 g_1\left(\theta_1 - \frac{1}{e_1} \ln |x_2|\right) \right). \end{aligned} \quad (9)$$

In this expression the sign of  $x_2$  determines which branch of the unstable manifold of  $P$  is followed (the positive branch to  $+E_2$  or the negative branch to  $-E_2$ ), while the notation  $\pm_3$  indicates whether the trajectory came from  $+E_3$  or  $-E_3$  prior to passing through  $H_1^{\text{in}}$ .

Next,  $C_2 \equiv \Psi_{23} \circ \phi_2 : H_2^{\text{in}} \rightarrow H_3^{\text{in}}$  is:

$$\begin{aligned} C_2(r_1 = h, \theta_1, \xi_2, x_3) &= \left( \tilde{x}_1 = \epsilon_1 a_r + A_2 |x_3|^{\delta_2} \cos \left( \theta_1 + \Phi_2 - \frac{1}{e_2} \ln |x_3| \right), \right. \\ &\quad \tilde{y}_1 = \epsilon_1 a_i + A_2 |x_3|^{\delta_2} \sin \left( \theta_1 + \Phi_2 - \frac{1}{e_2} \ln |x_3| \right), \\ &\quad \left. \tilde{x}_2 = \pm_2 h, \tilde{\xi}_3 = B_2 \right), \end{aligned} \quad (10)$$

where  $\tilde{x}_2 = \pm_2 h$  indicates whether the trajectory starts near  $+E_2$  or near  $-E_2$ , and the sign of  $x_3$  specifies whether the trajectory goes towards  $+E_3$  or  $-E_3$ .

Finally,  $C_3 \equiv \Psi_{31} \circ \phi_3 : H_3^{\text{in}} \rightarrow H_1^{\text{in}}$  is:

$$\begin{aligned} C_3(r_1, \theta_1, x_2 = \pm_2 h, \xi_3) &= \left( \tilde{\xi}_1 = B_3, \tilde{\theta}_1 = \theta_1 + \Phi_3 - \frac{1}{e_3} \ln r_1, \right. \\ &\quad \tilde{x}_2 = \pm_2 A_3 r_1^{\delta_3} \pm_2 \epsilon_1 r_1^{\delta_3} f_3 \left( \theta_1 - \frac{1}{e_3} \ln r_1 \right) \\ &\quad \left. + \epsilon_2 + \epsilon_1 \epsilon_2 g_3 \left( \theta_1 - \frac{1}{e_3} \ln r_1 \right), \right. \\ &\quad \left. \tilde{x}_3 = \pm_3 h \right), \end{aligned} \quad (11)$$

where  $\tilde{x}_3 = \pm_3 h$  shows whether the trajectory starts near  $+E_3$  or near  $-E_3$ , and  $\pm_2$  specifies which of  $\pm_2 E_2$  the trajectory came from prior to visiting  $\pm_3 E_3$ .

A return map can be obtained by composing  $C_1$ ,  $C_2$  and  $C_3$  in the appropriate order. To minimise complications due to the change from Cartesian to polar coordinates in going from  $C_2$  to  $C_3$ , we define the return map on  $H_3^{\text{in}}$ , i.e.,  $R \equiv C_2 \circ C_1 \circ C_3 : H_3^{\text{in}} \rightarrow H_3^{\text{in}}$ . We obtain different forms of  $R$  depending on which symmetries are broken.

First, in the case with full symmetry ( $\epsilon_1 = \epsilon_2 = \epsilon_3 = 0$ ), we have:

$$\begin{aligned} R(r_1, \theta_1, x_2 = \pm_2 h, \xi_3) &= \left( \tilde{r}_1 = A r_1^\delta, \tilde{\theta}_1 = \theta_1 + \Phi - Q \ln r_1, \right. \\ &\quad \left. \tilde{x}_2 = \pm_2 h, \tilde{\xi}_3 = B_2 \right), \end{aligned} \quad (12)$$

where  $A > 0$  and  $\Phi$  are constants,  $\delta = \delta_1 \delta_2 \delta_3$ , and  $Q = (e_1 e_2 + e_2 e_3 + e_3 e_1) / e_1 e_2 e_3$ . The trajectory returns near  $+E_3$  or  $-E_3$  according to the initial

sign of  $x_3$ . Since the symmetry  $\kappa_1$  is in force, we write the final point of this map in polar rather than Cartesian coordinates.

Second, breaking the  $\kappa_2$  and  $\kappa_3$  symmetries ( $\epsilon_1 = 0$ ,  $\epsilon_2 \neq 0$ ,  $\epsilon_3 \neq 0$ ) we have:

$$\begin{aligned} R(r_1, \theta_1, x_2 = \pm_2 h, \xi_3) &= \left( \tilde{r}_1 = A_2 \left| \epsilon_3 \pm_3 A_1 \left| \epsilon_2 \pm_2 A_3 r_1^{\delta_3} \right|^{\delta_1} \right|^{\delta_2}, \right. \\ \tilde{\theta}_1 &= \theta_1 + \Phi_1 + \Phi_2 + \Phi_3 - \frac{1}{e_3} \ln r_1 \\ &\quad - \frac{1}{e_1} \ln \left| \epsilon_2 \pm_2 A_3 r_1^{\delta_3} \right| \\ &\quad \left. - \frac{1}{e_2} \ln \left| \epsilon_3 \pm_3 A_1 \left| \epsilon_2 \pm_2 A_3 r_1^{\delta_3} \right|^{\delta_1} \right|, \right. \\ \tilde{x}_2 &= \operatorname{sgn} \left( \epsilon_2 \pm_2 A_3 r_1^{\delta_3} \right) h, \tilde{\xi}_3 = B_2 \Big), \end{aligned} \quad (13)$$

where the trajectory ends up near  $+E_3$  or  $-E_3$  according to the sign of  $\epsilon_3 \pm_3 A_1 \left| \epsilon_2 \pm_2 A_3 r_1^{\delta_3} \right|^{\delta_1}$ .

Third, if we break the  $\kappa_1$  symmetry but preserve  $\kappa_2$  and  $\kappa_3$  ( $\epsilon_1 \neq 0$ ,  $\epsilon_2 = \epsilon_3 = 0$ ) we have:

$$\begin{aligned} R(r_1, \theta_1, x_2 = \pm_2 h, \xi_3) &= \left( \tilde{x}_1 = \epsilon_1 a_r + A_2 |\hat{x}_3|^{\delta_2} \cos \hat{\theta}_1, \right. \\ \tilde{y}_1 &= \epsilon_1 a_i + A_2 |\hat{x}_3|^{\delta_2} \sin \hat{\theta}_1, \\ \tilde{x}_2 &= x_2, \tilde{\xi}_3 = B_2 \Big), \end{aligned} \quad (14)$$

where

$$\begin{aligned} \hat{x}_2 &= \pm_2 \left( A_3 + \epsilon_1 f_3 \left( \theta_1 - \frac{1}{e_3} \ln r_1 \right) \right) r_1^{\delta_3}, \\ \hat{x}_3 &= \pm_3 \left( A_1 + \epsilon_1 f_1 \left( \theta_1 + \Phi_3 - \frac{1}{e_3} \ln r_1 - \frac{1}{e_1} \ln |\hat{x}_2| \right) \right) |\hat{x}_2|^{\delta_1}, \\ \hat{\theta}_1 &= \theta_1 + \Phi_1 + \Phi_2 + \Phi_3 - \frac{1}{e_3} \ln r_1 - \frac{1}{e_1} \ln |\hat{x}_2| - \frac{1}{e_2} \ln |\hat{x}_3|. \end{aligned}$$

The trajectory ends up near  $+E_3$  or  $-E_3$  according to the sign of  $x_3$  since the subspace  $x_3 = 0$  is invariant. The map (14) can be simplified by assuming that  $A_3$  and  $A_1$  are order one and dropping the terms proportional to  $\epsilon_1$  in

the expressions for  $\hat{x}_2$  and  $\hat{x}_3$ . This results in an approximate map:

$$\begin{aligned} R(r_1, \theta_1, x_2 = \pm_2 h, \xi_3) &= \left( \tilde{x}_1 = \epsilon_1 a_r + A r_1^\delta \cos(\theta_1 + \Phi - Q \ln r_1), \right. \\ &\quad \tilde{y}_1 = \epsilon_1 a_i + A r_1^\delta \sin(\theta_1 + \Phi - Q \ln r_1), \\ &\quad \left. \tilde{x}_2 = x_2, \tilde{\xi}_3 = B_2 \right), \end{aligned} \quad (15)$$

where  $\delta$  and  $Q$  were defined above, and  $A$  and  $\Phi$  are constants as in equation (12).

Finally, when all symmetries are broken the return map is similar to the map (14) above, though with definitions of  $\hat{x}_2$  and  $\hat{x}_3$  that include terms proportional to  $\epsilon_2$  and  $\epsilon_3$  as in (11) and (9):

$$\begin{aligned} \hat{x}_2 &= \pm_2 \left( A_3 + \epsilon_1 f_3 \left( \theta_1 - \frac{1}{e_3} \ln r_1 \right) \right) r_1^{\delta_3} \\ &\quad + \epsilon_2 \left( 1 + \epsilon_1 g_3 \left( \theta_1 - \frac{1}{e_3} \ln r_1 \right) \right), \\ \hat{x}_3 &= \pm_3 \left( A_1 + \epsilon_1 f_1 \left( \theta_1 + \Phi_3 - \frac{1}{e_3} \ln r_1 - \frac{1}{e_1} \ln |\hat{x}_2| \right) \right) |\hat{x}_2|^{\delta_1} \\ &\quad + \epsilon_3 \left( 1 + \epsilon_1 g_1 \left( \theta_1 + \Phi_3 - \frac{1}{e_3} \ln r_1 - \frac{1}{e_1} \ln |\hat{x}_2| \right) \right), \\ \hat{\theta}_1 &= \theta_1 + \Phi_1 + \Phi_2 + \Phi_3 - \frac{1}{e_3} \ln r_1 - \frac{1}{e_1} \ln |\hat{x}_2| - \frac{1}{e_2} \ln |\hat{x}_3|. \end{aligned}$$

It might seem that terms proportional to  $\epsilon_1$  in  $\hat{x}_2$  and  $\hat{x}_3$  above could be dropped, as they were above. However, the terms  $\pm_2 A_3 r_1^{\delta_3}$  and  $\epsilon_2$  could nearly cancel and likewise  $\pm_3 A_1 |\hat{x}_2|^{\delta_1}$  and  $\epsilon_3$ , so we do not drop the  $\epsilon_1$  terms; in fact, it turns out that retaining the  $\epsilon_1$  terms is essential for understanding the switching mechanisms.

It is possible to write down equivalent maps from  $H_1^{\text{in}} \rightarrow H_1^{\text{in}}$  and  $H_2^{\text{in}} \rightarrow H_2^{\text{in}}$ . Note that the radial coordinates play no role in the return maps, at the order to which we are working.

## 4 Analysis of return maps

Behaviour in the case without symmetry breaking is well understood and simple: whenever  $\delta > 1$  and  $r$  is small, iteration of map (12) results in progressively smaller values of  $r$  and so there is an asymptotically stable heteroclinic cycle. The signs of  $x_2$  and  $x_3$  cannot change, owing to the presence of invariant subspaces, so each trajectory is confined to one quarter of the phase space. For the remainder of this section, we will assume  $\delta > 1$ .

### 4.1 Global bifurcations

Global bifurcations are a key ingredient for understanding the dynamics of the non-symmetric system. In this section, we describe the global bifurcations that are most important for our analysis of the system.

**4.1.1 Homoclinic bifurcation of  $P$ .** The periodic orbit  $P$  has stable and unstable manifolds of dimension three and two, respectively, meaning that transverse intersections of the manifolds, when they occur, do so in a codimension-zero way, while tangencies between the manifolds will be of codimension one. Transverse homoclinic orbits can only occur when all symmetries are broken, as the following argument shows. If  $\epsilon_2 = 0$ , the subspace  $x_2 = 0$  is invariant; since  $W^s(P)$  lies in that subspace it cannot intersect  $W^u(P)$ . Similarly, if  $\epsilon_3 = 0$ , the subspace  $x_3 = 0$  is invariant; since  $W^u(P)$  lies in that subspace it cannot intersect  $W^s(P)$ . If  $\epsilon_1 = 0$  then the rotation symmetry ensures that any intersection of  $W^u(P)$  and  $W^s(P)$  will not be transverse.

In the case  $\epsilon_1 = 0$ ,  $\epsilon_2 \neq 0$ ,  $\epsilon_3 \neq 0$ , non-transversal homoclinic orbits of  $P$  occur when one branch of the stable manifold of  $P$  is coincident with one branch of the unstable manifold of  $P$ . This event can be located in the return map by calculating the image of  $W^u(P)$  under  $C_3 \circ C_2 \circ \Psi_{12}$  and setting the  $x_2$  component of the image to zero, from which it is found that for small symmetry-breaking, non-transversal homoclinic bifurcations of  $P$  occur at

$$\epsilon_2 = -\pm_2 A_3 A_2^{\delta_3} |\epsilon_3|^{\delta_2 \delta_3}, \quad \epsilon_1 = 0. \quad (16)$$

Homoclinic orbits can be formed by coincidence of either of the two branches

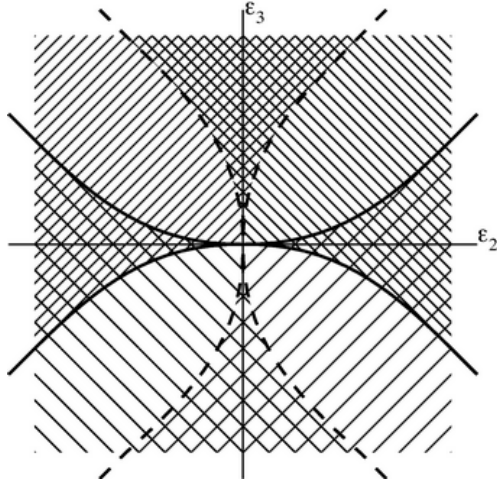


Figure 3. Schematic bifurcation set for the case  $\epsilon_1 = 0$ ,  $\epsilon_2$  and  $\epsilon_3$  small. Regions of asymptotically stable quasiperiodic solutions are bounded by codimension-one curves of global bifurcations, i.e., non-transverse homoclinic bifurcations of  $P$  (dashed curves) and heteroclinic bifurcations of the cycles  $\pm E_2 \rightarrow \pm E_3 \rightarrow \pm E_2$  (solid curves). The shapes of the global bifurcation curves correspond to the choice  $\delta_1 > 1$ ,  $\delta_2 > 1$  and  $\delta_3 > 1$ , but similar figures could be drawn for the other cases. As explained in Section 4.2, the various shading styles indicate the regions in which four different quasiperiodic solutions occur. Close to the  $\epsilon_2$  and  $\epsilon_3$  axes, two different quasiperiodic solutions coexist.

of  $W^u(P)$  with either of the two branches of  $W^s(P)$ , resulting in four possible homoclinic bifurcations corresponding to the four separate curves implicit in the expression above. These curves are shown as dashed lines in figure 3.

As  $\epsilon_1$  changes from zero, each curve (in parameter space) of non-transversal homoclinic bifurcations will generically split into two curves of homoclinic tangencies, with the region between the tangencies being parameter values for which there are transverse homoclinic orbits of  $P$ . The curves of homoclinic tangencies and regions of homoclinic tangles are shown schematically in figure 4.

Closer inspection of the expression for the  $x_2$  component of the image of  $W^u(P)$  under  $C_3 \circ C_2 \circ \Psi_{12}$  gives more information about loci of the homoclinic bifurcations of  $P$  when  $\epsilon_1 \neq 0$ . This component can be written as:

$$\tilde{x}_2 = \pm_2 R_1^{\delta_3} (A_3 + \epsilon_1 f_3(\Theta_1)) + \epsilon_2 (1 + \epsilon_1 g_3(\Theta_1)), \quad (17)$$

where  $R_1$  and  $\Theta_1$  are complicated functions of the coefficients and parameters. In this expression,  $A_3 + \epsilon_1 f_3(\Theta_1)$  must remain positive, as argued above, and

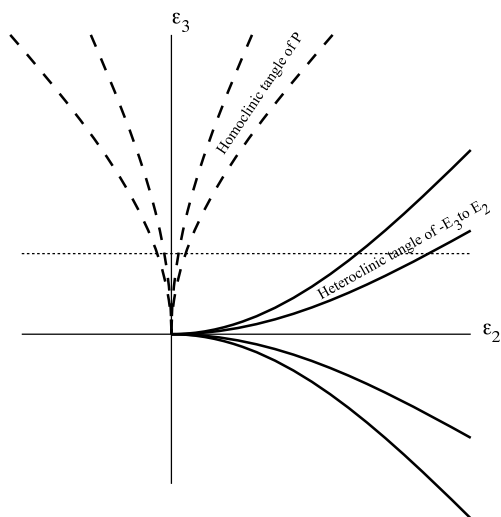


Figure 4. Schematic diagram showing part of the bifurcation set for the case  $\epsilon_1$  fixed and non-zero but small (compare with figure 3). Dashed curves correspond to homoclinic tangencies of  $P$ , solid curves in the first (resp. fourth) quadrant correspond to heteroclinic tangencies between  $W^u(-E_3)$  (resp.  $W^u(E_3)$ ) and  $W^s(E_2)$ . The dotted horizontal line indicates a path through parameter space discussed in Section 4.4.

$R_1$  is positive. Expressions for the positions of the homoclinic tangencies in parameter space can be calculated by setting  $\tilde{x}_2 = 0$ ; these expressions are not included here due to their extreme ugliness. Nonetheless, we note that for  $\epsilon_1$  small, when  $\pm_2 = +$ , there are only solutions with  $\epsilon_2 < 0$ ; this is consistent with figures 3 and 4, in which each bifurcation curve is confined to a single quadrant. However, if  $\epsilon_1$  is large enough that  $1 + \epsilon_1 g_3(\Theta_1)$  can change sign as  $\Theta_1$  varies, the loci of the homoclinic bifurcations of  $P$  can change quadrants. Of course, this effect is outside the range of validity of the return maps we have constructed, but the principle is worth bearing in mind as it appears to influence the dynamics observed in the numerical example discussed in Section 5.

**4.1.2 Heteroclinic bifurcation  $\pm E_2 \rightarrow \pm E_3 \rightarrow \pm E_2$ .** In the case that all symmetries are broken, consideration of the dimensions of the stable and unstable manifolds of  $E_2$  and  $E_3$  shows that the heteroclinic cycle  $E_2 \rightarrow E_3 \rightarrow E_2$  will occur in a codimension-two manner. However, if  $\epsilon_1 = 0$ , the connection  $E_2 \rightarrow E_3$  is robust and the intersection of  $W^u(E_3)$  and  $W^s(E_2)$  is a codimension-one phenomenon, meaning that the heteroclinic cycle as a

whole occurs with codimension one. This latter case is of interest since, as we will see, the heteroclinic bifurcation unfolds when  $\epsilon_1 \neq 0$  into homoclinic bifurcations of  $E_2$  and  $E_3$  and heteroclinic tangencies between  $W^u(E_3)$  and  $W^s(E_2)$  similar to the way each non-transverse homoclinic bifurcation of  $P$  splits into two homoclinic tangencies when  $\epsilon_1$  is varied from zero (see above). An analogous argument works for heteroclinic cycles involving  $-E_2$  and/or  $-E_3$ .

Calculations with the local and global maps yields an expression for the parameter values at which these heteroclinic bifurcations occur:

$$\epsilon_3 = -\pm_3 A_1 |\epsilon_2|^{\delta_1}, \quad \epsilon_1 = 0.$$

See figure 3. This expression is valid for all four cycles  $\pm E_2 \rightarrow \pm E_3 \rightarrow \pm E_2$  so long as  $\pm_3$  and the sign of  $\epsilon_2$  are chosen appropriately.

**4.1.3 Homoclinic bifurcations of  $\pm E_2$  and  $\pm E_3$ .** The dimensions of the stable and unstable manifolds of  $E_2$  and  $E_3$  are such that if homoclinic bifurcations of these equilibria occur, they are of codimension one.

An argument similar to that used in subsection 4.1.1 shows that we require  $\epsilon_1 \neq 0$  and  $\epsilon_3 \neq 0$  if a homoclinic bifurcation of  $E_2$  is to occur, although  $\epsilon_2$  could be zero. Similarly, existence of a homoclinic bifurcation of  $E_3$  requires  $\epsilon_1 \neq 0$  and  $\epsilon_2 \neq 0$ , although  $\epsilon_3$  could be 0. The homoclinic bifurcation of  $E_2$  (resp.  $E_3$ ) will be of Shil'nikov type if  $\delta_2 < 1$  (resp.  $\delta_3 < 1$ ) and if  $c_2 < 2$  (resp.  $c_3 < 2$ ) [30].

We can in principle calculate parameter values at which these homoclinic bifurcations occur, but the expressions are too nasty to be useful. Instead, we note that there can be two homoclinic bifurcations of  $E_2$ , one for each branch of the unstable manifold of  $E_2$ , and a further two homoclinic bifurcations of  $-E_2$ . Similarly, there can be two homoclinic bifurcations of  $E_3$  and two homoclinic bifurcations of  $-E_3$ . These eight homoclinic bifurcations will in general occur at different parameter values, but in the limit  $\epsilon_1 \rightarrow 0$ , will converge pairwise on the loci of the four heteroclinic bifurcations involving  $\pm E_2$  and  $\pm E_3$  discussed in the previous subsection. For instance, as  $\epsilon_1 \rightarrow 0$ , a homoclinic orbit of  $E_2$  passing near  $-E_3$  and a homoclinic orbit of  $-E_3$  passing near  $E_2$  will converge in phase space on the heteroclinic cycle  $E_2 \rightarrow -E_3 \rightarrow E_2$ , and the parameter



values at which the homoclinic bifurcations occur will converge in parameter space on the locus of the heteroclinic bifurcation. For clarity, these bifurcation curves are not shown in figure 4.

The dynamics associated with the global bifurcations described above will be discussed further below.

#### 4.2 Breaking the two reflection symmetries

In this subsection, we show that, for  $\epsilon_1 = 0$  and for sufficiently small  $\epsilon_2$  and  $\epsilon_3$ , the map (13) generically has at least one asymptotically stable closed invariant curve and the corresponding flow has quasiperiodic solutions.

The  $r_1$  component of the map (13) is independent of the other variables. We seek values of  $r_1$  for which  $F(r_1) = r_1$ , where

$$F(r_1) = A_2 \left| \epsilon_3 \pm_3 A_1 |\epsilon_2 \pm_2 A_3 r_1^{\delta_3}|^{\delta_1} \right|^{\delta_2}, \quad (18)$$

by considering possible intersections of the graph of  $F(r_1)$  with the diagonal. For each choice of  $\epsilon_2$  and  $\epsilon_3$ , there are two possible signs of each of  $\pm_2$  and  $\pm_3$ , corresponding to different potential fixed points. However, the case  $(\pm_2 = +, \epsilon_2 > 0)$  is equivalent to  $(\pm_2 = -, \epsilon_2 < 0)$ , and the case  $(\pm_3 = +, \epsilon_3 > 0)$  is equivalent to  $(\pm_3 = -, \epsilon_3 < 0)$ . Without loss of generality, we therefore focus on the case  $\pm_2 = +$  and  $\pm_3 = +$ , and examine the ranges of  $\epsilon_2$  and  $\epsilon_3$  (positive or negative) for which fixed points of map (18) exist and are stable. Note that fixed points of this type must have positive values within the absolute value signs in expression (18), since the signs of  $\epsilon_2 + A_3 r_1^{\delta_3}$  and  $\epsilon_3 + A_1 |\epsilon_2 + A_3 r_1^{\delta_3}|^{\delta_1}$  determine the next values of  $\pm_2$  and  $\pm_3$ .

For all sufficiently small and positive  $\epsilon_2$  and  $\epsilon_3$ ,  $F(0) = A_2(\epsilon_3 + A_1 \epsilon_2^{\delta_1})^{\delta_2} > 0$ . For  $r_1$  larger than  $\epsilon_2$  and  $\epsilon_3$  but still smaller than one, we have  $F(r_1) \sim r_1^\delta$ , which is less than  $r_1$  since  $\delta > 1$ . Thus, by continuity, the map has a fixed point (see figure 5(b)). Since  $F(r_1)$  is a monotonically increasing function, the slope of  $F$  at the fixed point is less than one, so the fixed point exists and is stable in the quadrant  $\epsilon_2 > 0, \epsilon_3 > 0$ .

This fixed point (i.e., a fixed point with  $\pm_2 = \pm_3 = 1$ ) also exists in some parts of the second and fourth quadrants of the  $(\epsilon_2, \epsilon_3)$  parameter plane. To determine the region of existence of the fixed point in the fourth quadrant,

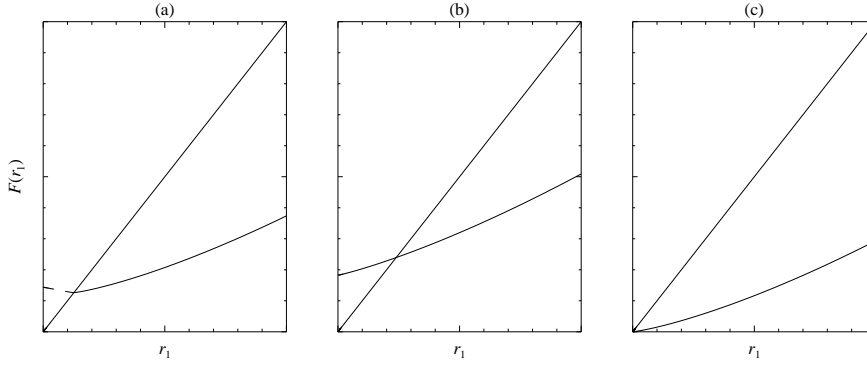


Figure 5. Schematic graphs of  $F(r_1)$  (defined by equation (18)) against  $r_1$  for the choice  $\pm_2 = \pm_3 = 1$  in the case that  $\delta_1 > 1$ ,  $\delta_2 > 1$ ,  $\delta_3 > 1$ , and  $A_1 = A_2 = A_3 = 1$ . The solid (resp. dashed) curve indicates values of  $r_1$  for which the next values of  $\pm_2$  and  $\pm_3$  are (resp. are not) both positive; we seek values of  $r_1$  for which the solid curve intersects the diagonal. For small and positive  $\epsilon_2$  and  $\epsilon_3$ , a stable fixed point exists (see panel (b)). This fixed point ceases to exist in the second quadrant when  $\epsilon_2 = -A_3 A_2^{\delta_2} \epsilon_3^{\delta_2 \delta_3}$ , when there is a non-transversal homoclinic bifurcation of  $P$  (limiting case shown in panel (a)). The fixed point is destroyed in the fourth quadrant when  $\epsilon_3 = -A_1 \epsilon_2^{\delta_1}$ , when there is a non-transversal heteroclinic connection from  $E_3$  to  $E_2$  (limiting case shown in panel (c)).

we fix  $\epsilon_2$  to be some small positive value and decrease  $\epsilon_3$  to negative values. This has the effect of shifting the graph of  $F(r_1)$  down, from which it is easy to see that the fixed point exists and is stable until  $F(0) = 0$ , i.e., until  $\epsilon_3 = -A_1 \epsilon_2^{\delta_1}$ . The graph of  $F(r_1)$  in the case  $\epsilon_3 = -A_1 \epsilon_2^{\delta_1}$  is shown schematically in figure 5(c). The parameter values at which the fixed point ceases to exist in the fourth quadrant coincides with the locus on which the heteroclinic bifurcation from  $E_3$  to  $E_2$  exists (see section 4.1.2).

To determine the region of existence of the fixed point in the second quadrant, we now fix  $\epsilon_3$  at some small positive value and decrease  $\epsilon_2$  until it becomes negative. As  $\epsilon_2$  decreases,  $F(0)$  decreases and the shape of the graph of  $F(r_1)$  also changes; the graph remains monotonic increasing in  $r_1$  while  $\epsilon_2$  is positive, but once  $\epsilon_2$  becomes negative, the graph has a turning point, with  $F(r_1)$  decreasing for  $r_1$  near zero. The decreasing section is indicated by a dashed curve in figure 5(a), and corresponds to future values of  $\pm_2$  and  $\pm_3$  not both being positive. For small enough negative  $\epsilon_2$  the dashed section of the graph lies to the left of the intersection of the graph with the diagonal, but when  $\epsilon_2 = -A_3 A_2^{\delta_2} \epsilon_3^{\delta_2 \delta_3}$ , the dashed curve reaches to the diagonal and the fixed point ceases to exist. The graph of  $F(r_1)$  in the case  $\epsilon_2 = -A_3 A_2^{\delta_2} \epsilon_3^{\delta_2 \delta_3}$  is shown schematically in figure 5(a). The parameter values at which the fixed

point ceases to exist in the second quadrant coincides with the locus on which there is a homoclinic bifurcation of  $P$  (see section 4.1.1).

Thus we find that a stable fixed point of the equation  $F(r_1) = r_1$  exists in a region of the  $(\epsilon_2, \epsilon_3)$  parameter space containing all the first quadrant and parts of the second and fourth quadrants, with the region of existence being bounded by the loci of certain global bifurcations. The region of existence of this fixed point is indicated by the region of left-leaning close hatching in figure 3. Calculations with the other choices of signs of  $\pm_2$  and  $\pm_3$  are analogous, and yield different regions of existence for the corresponding fixed points. These regions coexist as shown by the regions with different hatching styles in figure 3.

Now consider the  $\theta$  component of the map (13). For fixed  $r_1$ , this component is a rigid rotation in  $\theta_1$ . Thus, a fixed point of equation (18) generically corresponds to a closed invariant curve in the map (13), and, generically, a quasiperiodic solution in the underlying flow. In the flow, as in the map, the angle  $\theta_1$  decouples from the rest of the dynamics, and so for a dense set of parameter values, the full flow could instead have an invariant torus foliated by periodic orbits. Stability of these quasiperiodic solutions follows from the stability of the fixed point of (18).

The calculations above were all for the case that  $\delta_1 > 1$ ,  $\delta_2 > 1$ ,  $\delta_3 > 1$ . Similar, but more complicated calculations can be done in the case that one or more of the  $\delta_i$  is smaller than one. This leads to similar regions of existence of the fixed points, except that there will be additional saddle-node bifurcations of the fixed points close to the relevant global bifurcations; these saddle-node bifurcations are necessary since the global bifurcations destroy quasiperiodic solutions of different stabilities depending on the sign of  $\delta_i - 1$ .

The special case that precisely one of  $\epsilon_2$  and  $\epsilon_3$  is zero (i.e., only one reflection symmetry is broken) is covered by the analysis above; there will be two fixed points of the map with corresponding (foliated) tori in the flow.

In summary, when we preserve the rotation symmetry and break the two reflection symmetries, the flow will generically have asymptotically stable quasiperiodic solutions that do not exhibit switching. There are regions where there are coexisting stable quasiperiodic solutions, and these regions are bounded by global bifurcations that will play an important role in generating complex dynamics when  $\epsilon_1 \neq 0$ .

### 4.3 Breaking the rotation symmetry

In this subsection we show that for sufficiently small values of  $\epsilon_1$ , with  $\epsilon_2 = \epsilon_3 = 0$ , the map (15) has a stable fixed point.

By rescaling  $r_1$  and  $\epsilon_1$  by order one amounts and moving the origin of the  $\theta_1$  coordinate, we can without loss of generality set  $A = 1$ ,  $a_r = 1$  and  $a_i = 0$  in (15). Ignoring for now the  $x_2$  and  $\xi_3$  components of the map and working with polar coordinates  $(\rho, \phi)$  centred at  $(x_1, y_1) = (\epsilon_1, 0)$  (so that  $x_1 = \epsilon_1 + \rho \cos \phi$  and  $y_1 = \rho \sin \phi$ ), map (15) reduces to

$$\begin{cases} \tilde{x}_1 = \epsilon_1 + \tilde{\rho} \cos \tilde{\phi} \\ \tilde{y}_1 = \tilde{\rho} \sin \tilde{\phi} \end{cases} \quad \text{where} \quad \begin{cases} \tilde{\rho} = r_1^\delta \\ \tilde{\phi} = \theta_1 + \Phi - Q \ln r_1. \end{cases} \quad (19)$$

The constant  $\Phi$  may take a different value here than in equations (15). Fixed points of (19) satisfy  $r_1 = \sqrt{\tilde{x}_1^2 + \tilde{y}_1^2}$  and  $\theta_1 = \arctan(\tilde{y}_1/\tilde{x}_1)$ . To find solutions of the first of these equations, note that circles of radius  $r$  about  $(x_1, y_1) = (0, 0)$  map under (19) to circles of radius  $r^\delta$  about  $(\epsilon_1, 0)$ . Since  $\delta > 1$  and for small  $r$ , these circles will intersect if  $r \geq \epsilon_1 - r^\delta$  and  $r \leq \epsilon_1 + r^\delta$ ; the intersection points are candidate fixed points of the map. For each small fixed value of  $\epsilon_1$ , there will be some non-zero interval  $a \leq r \leq b$  on which the inequalities are both satisfied. See figure 6(a–c).

The second equation,  $\theta_1 = \arctan(\tilde{y}_1/\tilde{x}_1)$ , is satisfied for at least one value of  $r$  in  $[a, b]$ , as the following argument shows. When  $r = a$ , the circles  $(r_1, \theta_1) = (r, \theta_1)$  and  $(\rho, \phi) = (r^\delta, \phi)$  intersect at a single point,  $(r_1, \theta_1) = (a, 0)$ , alternatively  $(\rho, \phi) = (a^\delta, \pi)$ . As  $r$  is increased beyond  $a$ , the intersection point splits into two points (with corresponding  $\phi$  values just below  $\pi$  and just above  $-\pi$ ). The intersection points come together again at  $(r_1, \theta_1) = (b, 0)$  or  $(\rho, \phi) = (b^\delta, 0)$ , in the manner shown in figure 6(d). The corresponding value of  $\tilde{\phi}$  for each intersection point can be calculated from (19) (see figure 6(e)) from which it is seen that the two branches of  $\tilde{\phi}$ , arising from the upper and lower intersections of the two circles, start and end at the same point as each other, as shown in figure 6(f). At least one of the two branches of the graph of  $\tilde{\phi}$  vs  $r$  therefore intersects the graph of  $\phi$  vs  $r$  for that same branch for at least one  $r$  in  $[a, b]$ . We conclude that there is at least one fixed point of the map (19).

It is straightforward to show that the determinant of the Jacobian of

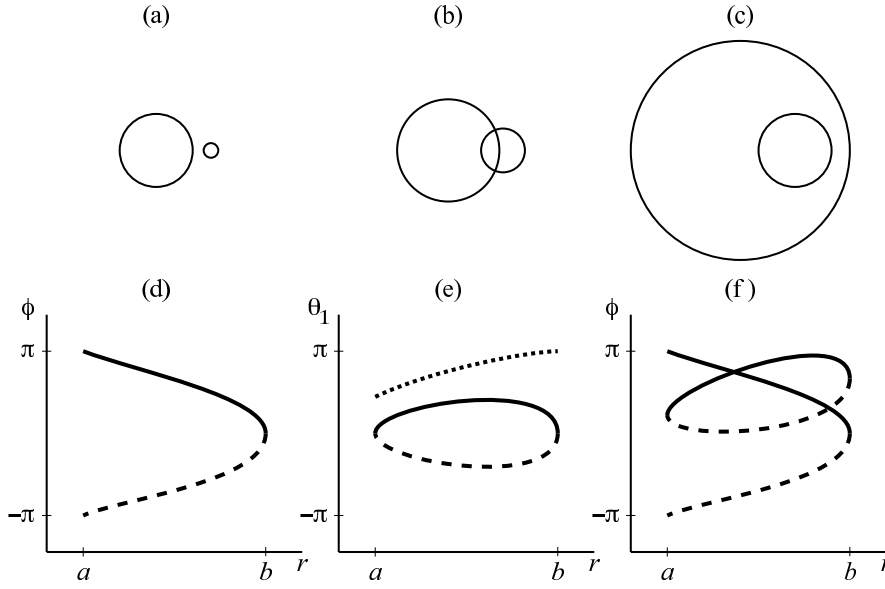


Figure 6. Finding fixed points of equations (19). Panels (a)-(c) show schematically the relative positions of the circle of radius  $r$  around  $(x_1, y_1) = (0, 0)$  (large circle in each panel) and its image under map (19) for various sizes of  $r$ : (a)  $r < \epsilon_1 - r^\delta$ , no intersection; (b)  $r \geq \epsilon_1 - r^\delta$  and  $r \leq \epsilon_1 + r^\delta$ , one or two intersections; (c)  $r > \epsilon_1 + r^\delta$ , no intersections. (d) Schematic  $\phi$  values for intersections of the two circles  $(r_1, \theta_1) = (r, \theta_1)$  and  $(\rho, \phi) = (r^\delta, \phi)$ , in the situation shown in case (b), plotted as a function of  $r$ ; (e) Schematic showing  $\theta_1$  (solid and dashed curves) and  $-Q \ln r_1$  (dotted curve) for points of intersection of the two circles, plotted as a function of  $r$  at the intersection points; (f)  $\phi$  and  $\tilde{\phi}$  values at points of intersection of the two circles. In panels (d)-(f), solid curves correspond to the upper intersection points and their images, dashed curves correspond to the lower intersection points and their images.

map (19) is  $\delta r^{2(\delta-1)}$  and that the absolute value of the trace of the Jacobian is bounded above by  $\sqrt{(\delta+1)^2 + Q^2} r^{\delta-1}$ . For each choice of  $\epsilon_1$ , the value of  $r$  at the corresponding fixed point lies in  $[a, b]$ , where  $a$  and  $b$  depend on  $\epsilon_1$  with  $a > 0$  and  $a$  and  $b$  tending to zero as  $\epsilon_1 \rightarrow 0$ . Thus, for sufficiently small  $\epsilon_1$ , the determinant and trace of the linearised map will be small enough to ensure that the relevant fixed point is stable. It follows that the corresponding fixed point of map equations (15) is also stable, since orbits of that map collapse onto a constant value of the third (radial) coordinate after one iteration of the map.

Thus for sufficiently small  $\epsilon_1$  when  $\epsilon_2 = \epsilon_3 = 0$ , the heteroclinic cycle that occurred in the fully symmetric case is replaced by a stable periodic orbit. Using the reflection symmetries  $\kappa_2$  and  $\kappa_3$ , we find four stable periodic orbits co-exist, one in each quarter of the phase space.

#### 4.4 *Breaking all symmetries*

Direct analysis of the return map valid for the case that all symmetries are broken is not feasible because of the extremely complicated form of that map. Instead, in this section we use our knowledge of the dynamics in the case  $\epsilon_1 = 0$  and arguments about generic unfoldings of this special case to deduce what types of dynamics will be seen in the fully asymmetric case for  $\epsilon_1$  near zero, and to (approximately) locate each type of behaviour in parameter space. This procedure allows us to make specific predictions about the mechanisms underlying the complicated dynamics observed in numerical examples, such as the example described in section 5. We are especially interested in finding mechanisms that cause repeated, non-periodic switching in our system.

The dynamics associated with the case  $\epsilon_1 = 0$  is summarised in figure 3, which shows eight curves of global bifurcations bounding regions in which there are asymptotically stable quasiperiodic solutions. In this case the rotation symmetry prevents coupling of the two frequencies associated with each quasiperiodic solution and the dynamics is simple. Once  $\epsilon_1$  moves away from zero, we will generically see locking of the frequencies. For instance, if we were to fix  $\epsilon_1$  sufficiently small but non-zero and pick  $\epsilon_2$  and  $\epsilon_3$  positive and with values midway between the two pairs of global bifurcation curves in the first quadrant of figure 4, then along a one-dimensional path through the parameter space such as the dotted line in figure 4 there will be intervals of quasiperiodicity interspersed with intervals of locked, periodic behaviour. Associated with the frequency locking there may be complicated dynamics such as period-doubling cascades and chaotic dynamics. However, this behaviour will mostly be confined to regions of phase space near the original quasiperiodic solutions, and is not the main mechanism for switching in our system.

As described in section 4.1.1 and shown in figure 4, each curve of non-transverse homoclinic bifurcations of  $P$  seen in figure 3 turns into a wedge in parameter space of transverse homoclinic orbits of  $P$  (a ‘homoclinic tangle’) when  $\epsilon_1$  changes from zero. There will be horseshoes and chaotic dynamics associated with the transverse homoclinic orbits, although the chaos may not be attracting. In numerical examples we might expect to see a mixture of stable periodic orbits and stable chaotic dynamics, in overlapping regions of parameter space.

An interesting consequence of the existence of homoclinic tangles in certain

regions of the parameter space is that it provides a mechanism for switching of orbits with respect to the  $x_2$  variable. For instance, for sufficiently small  $\epsilon_1$ , and with  $\epsilon_2 > 0$ ,  $\epsilon_3 > 0$  and both small, solutions that make excursions near  $E_2$  can get trapped; the trapping region is bounded in part by one branch of  $W^s(P)$  and trapped solutions make excursions past  $E_2$  but cannot cross  $W^s(P)$  so cannot get close to  $-E_2$ . If  $\epsilon_2$  is decreased, say by moving along the dotted path shown in Figure 4 into the homoclinic wedge in the second quadrant, the trapping region develops a leak when a homoclinic tangency forms between that branch of  $W^s(P)$  and a branch of  $W^u(P)$ ; solutions are then able to cross  $W^s(P)$ , and may visit a neighbourhood of  $-E_2$ . We call this ‘switching in  $x_2$ ’. Switching of this type (from positive to negative  $x_2$ ) can occur for parameter values to the left of the right boundary of the homoclinic wedge in the second quadrant.

Once a switching solution arrives in the region with  $x_2 < 0$ , it may then get captured by an attractor lying solely in the negative  $x_2$  region of phase space, in which case no more switching will be observed. Alternatively, if there is a mechanism for orbits to leak back to the original region of phase space then there could be sustained switching in  $x_2$ . This latter case cannot occur for arbitrarily small  $\epsilon_1$  as the following argument shows. For the case  $\epsilon_1 = 0$ , results from section 4.2 show that orbits which make repeated excursions near  $-E_2$  and  $E_3$  occur in the second quadrant of figure 4 and in the first quadrant as far as the locus of homoclinic bifurcations of  $P$ . (This homoclinic bifurcation involves a different branch of  $W^u(P)$  than the homoclinic bifurcation occurring for  $\epsilon_2 < 0$  discussed in the last paragraph.) For small  $\epsilon_1$ , there will be a wedge of homoclinic tangencies of the relevant branches of  $W^u(P)$  and  $W^s(P)$ , with the wedge lying entirely within the region  $\epsilon_2 > 0$ ,  $\epsilon_3 > 0$ ; orbits that make a number of excursions past  $-E_2$  before switching and passing close to  $E_2$  can only occur for values of  $\epsilon_2$  and  $\epsilon_3$  lying to the right of the left boundary of the wedge. Thus, for sufficiently small  $\epsilon_1$ , there is no overlap between the region of parameter space where there is switching from positive to negative  $x_2$  and the region where there is switching from negative to positive  $x_2$ , with the consequence that there can be no sustained switching in  $x_2$ .

However, as argued in section 4.1.1, for large enough  $\epsilon_1$  the curves of homoclinic tangency may change quadrants in the  $(\epsilon_2, \epsilon_3)$  parameter plane, and then the switching regions can overlap, making sustained switching in  $x_2$  pos-

sible. As pointed out in section 4.1.1, our return map construction is not valid for ‘large’  $\epsilon_1$ , so we have not proved the existence of sustained switching, just shown how it might feasibly occur. It is not possible to determine a priori how big  $\epsilon_1$  would have to be to get sustained switching, but we have shown that there is a threshold in  $\epsilon_1$  below which sustained switching in  $x_2$  is not possible. The value of this threshold does not go to zero as  $\epsilon_2$  and  $\epsilon_3$  go to zero, as it comes from the requirement that  $1 + \epsilon_1 g_3(\Theta_1)$  change sign (as a function of  $\Theta_1$ ) in equation (17). Another way of understanding this is to note that in (17), if  $\pm_2 = +$  and  $\epsilon_2 > 0$ , then the only way of having  $\tilde{x}_2$  negative is to have  $1 + \epsilon_1 g_3(\Theta_1) < 0$  for some value of  $\Theta_1$ . This is a necessary but not sufficient condition, as the attractor may not explore the required range of  $\Theta_1$ .

The four curves of heteroclinic bifurcations of the cycles  $\pm E_2 \rightarrow \pm E_3 \rightarrow \pm E_2$  shown in figure 3 also split when  $\epsilon_1$  becomes non-zero, being replaced by eight curves of homoclinic bifurcations and eight curves of heteroclinic tangencies between  $W^u(\pm E_3)$  and  $W^s(\pm E_2)$ , as described in section 4.1.2. The homoclinic bifurcations can complicate the dynamics by inducing chaotic dynamics if the homoclinic orbits are of Shil’nikov type, while the heteroclinic bifurcations are associated with switching in the  $x_3$  coordinate similarly to the way switching in  $x_2$  is associated with homoclinic bifurcations of  $P$ , described above. More precisely, the eight curves of heteroclinic tangencies between  $W^u(\pm E_3)$  and  $W^s(\pm E_2)$  come in pairs, with each pair bounding a wedge in parameter space. At parameter values within each wedge there is a heteroclinic tangle of one pair of manifold branches. For instance, for sufficiently small  $\epsilon_1$  there will be a heteroclinic wedge involving one branch of  $W^u(E_3)$  and one branch of  $W^s(E_2)$  occurring in the fourth quadrant in the  $(\epsilon_2, \epsilon_3)$  plane. Above this wedge,  $W^s(E_2)$  bounds in part a trapping region; orbits in the trapping region make excursions past  $E_3$  but cannot cross  $W^s(E_2)$  and cannot therefore get close to  $-E_3$ . The trapping region develops a leak when a heteroclinic tangency forms between the appropriate branches of  $W^u(E_3)$  and  $W^s(E_2)$  and solutions are then able to cross  $W^s(E_2)$ . We call this ‘switching in  $x_3$ ’. An argument analogous to that used above for switching in  $x_2$  can also be used here to show that there is a different threshold in  $\epsilon_1$  below which there can be no persistent switching in  $x_3$ . Again, this threshold does not go to zero as  $\epsilon_2$  and  $\epsilon_3$  go to zero.

The mechanisms inducing switching in  $x_2$  and in  $x_3$  are distinct, but or-



bits that switch persistently in both  $x_2$  and  $x_3$  are possible for  $\epsilon_1$  above the thresholds for both mechanisms. Switching in each variable requires the rotation and appropriate reflection symmetry to be broken. It is possible to have persistent switching in  $x_2$  with  $\epsilon_3 = 0$ , or switching in  $x_3$  with  $\epsilon_2 = 0$ , though we will not explore this possibility in detail. The example in section 5 shows that persistent switching is easily observed in numerical examples.

Both of the global bifurcations we have identified as inducing switching, i.e., homoclinic tangencies of  $W^u(P)$  and  $W^s(P)$  and heteroclinic tangencies of  $W^u(\pm E_3)$  and  $W^s(\pm E_2)$ , will produce horseshoes in the dynamics. In the case of homoclinic tangencies, this is a standard result and in the case of the heteroclinic tangencies, reinjection into the neighbourhood of the heteroclinic tangle is provided by proximity in phase and parameter space to the heteroclinic cycle  $\pm E_2 \rightarrow \pm E_3 \rightarrow \pm E_2$ . In either case, we therefore expect the onset of switching to be commonly associated with nearby chaotic dynamics; chaotic orbits before the onset of switching, chaotic transients for switching orbits and orbits that switch chaotically might all be seen. However, we note that other types of switching are also possible, such as periodic switching where the attractor is a periodic orbit that crosses the (non-invariant) hyperplanes  $x_2 = 0$  and  $x_3 = 0$  or periodic switching where the attractor is a ‘noisy periodic orbit’ such as results from a cascade of period doubling. In the latter case the itinerary of visits to  $\pm x_2$  or  $\pm x_3$  will be periodic even though the actual orbits are not.

## 5 Example

We consider the following system of equations to illustrate the dynamics of interest in this paper:

$$\dot{z}_1 = (1 + i)z_1 - |z_1|^2 z_1 - (c_2 + 1)x_2^2 z_1 + (e_3 - 1)x_3^2 z_1 + \epsilon_1 d_{11} + \epsilon_1 d_{12} x_1, \quad (20)$$

$$\dot{x}_2 = x_2 - x_2^3 - (c_3 + 1)x_3^2 x_2 + (e_1 - 1)|z_1|^2 x_2 + \epsilon_2 d_{21} + \epsilon_1 d_{22} x_1 x_2 + \epsilon_1 \epsilon_2 d_{23} x_1, \quad (21)$$

$$\dot{x}_3 = x_3 - x_3^3 - (c_1 + 1)|z_1|^2 x_3 + (e_2 - 1)x_2^2 x_3 + \epsilon_3 d_{31} + \epsilon_1 d_{32} x_1 x_3 + \epsilon_1 \epsilon_3 d_{33} x_1, \quad (22)$$

These equations were derived by starting with the structurally stable heteroclinic cycle considered in [2] and turning one equilibrium of that cycle into a periodic orbit by adding a trivial phase variable. The simplest possible terms that break the symmetries in generic ways were then added. In writing down these equations, we have used the same notation as was used in the maps derived earlier in this paper. In particular, the parameters  $\epsilon_1$ ,  $\epsilon_2$  and  $\epsilon_3$  in equations (20–22) play the same role as in the maps.

The model written down by [19] is similar, but ours differs in two respects. First, the symmetry-breaking terms in [19] were fifth-order in the  $x$  and  $z$  variables, rather than constant, linear and quadratic here. Second, the model in [19] respects the symmetry  $(z_1, x_2, x_3) \rightarrow (-z_1, -x_2, -x_3)$ , which is appropriate for a model of a dynamo instability: the invariant subspace  $z_1 = x_2 = x_3 = 0$  corresponds to the absence of any magnetic field. We do not expect the first difference between the models to alter the qualitative behaviour, but the enforced symmetry does have a significant effect, which we will not discuss in any detail.

The coefficients in the equations were chosen to be:  $c_1 = 1.2$ ,  $e_1 = 1.0$ ,  $c_2 = 1.1$ ,  $e_2 = 1.0$ ,  $c_3 = 1.1$ ,  $e_3 = 1.0$  for the contracting and expanding eigenvalues, and  $d_{11} = d_{12} = 10^{-4}$ ,  $d_{21} = 10^{-1}$ ,  $d_{22} = 10^{-1}$ ,  $d_{23} = 10^3$ ,  $d_{31} = 10^{-3}$ ,  $d_{32} = 10^{-4}$ ,  $d_{33} = 1$  for the symmetry-breaking coefficients. The eigenvalues were chosen to be of order one, with contraction dominating expansion at each point ( $\delta_1 = 1.2$ ,  $\delta_2 = 1.1$ ,  $\delta_3 = 1.1$ , and an overall  $\delta = 1.452$ ) The behaviour when not all ratios are greater than one (but  $\delta > 1$ ) is similar. The symmetry breaking coefficients are notionally small, but those coefficients ( $d_{23}$  and  $d_{33}$ ) that are multiplied by two  $\epsilon$ 's were chosen to be larger to compensate for this. The exact numbers are not important, though they will affect the details of what is observed.

We integrated the equations numerically using the Bulirsch–Stoer adaptive integrator [32], with a tolerance for the relative error set to  $10^{-12}$  for each step. Poincaré sections were computed using algorithms from [33].

By varying  $\epsilon_1$ ,  $\epsilon_2$  and  $\epsilon_3$ , we are able to find examples of the important symmetry-breaking effects discussed in the previous sections of this paper. The cases with full or partial symmetry preserved give straightforward results, which we describe only briefly; more details are provided of the case of fully broken symmetry.

If all symmetries are preserved (all  $\epsilon_i = 0$ ) then each solution starting off the invariant subspaces is attracted to one of four structurally stable heteroclinic cycles (the four cycles are related by the reflection symmetries). If  $\epsilon_1 \neq 0$ ,  $\epsilon_2 = \epsilon_3 = 0$  (rotation symmetry broken, reflections preserved), numerics confirm the predictions of section 4.3, and a single attracting periodic orbit is found in each quarter of the phase space. If rotation symmetry is preserved as well as one reflection, and the other reflection is broken, then solutions are attracted to a foliated torus, as discussed in section 4.2. In the case that both reflections are broken but the rotation symmetry is preserved, numerics confirm the predictions of section 4.2; we find that there exist attracting quasiperiodic solutions in regions bounded by curves of global bifurcations, as shown schematically in figure 3. Analysis of the maps derived earlier allows us to predict scaling of the loci of various global bifurcations in the limit of small symmetry breaking. For instance, equation (16) tells us that for  $\epsilon_1 = 0$  and  $\epsilon_3 \rightarrow 0$ , homoclinic bifurcations of  $P$  associated with equations (20–22) occur for  $\epsilon_2 = \text{constant} \times |\epsilon_3|^{\delta_2 \delta_3}$  but the value of the constant is not determined by the map analysis. Numerical simulations of equations (20–22) confirm the scalings for the various global bifurcations.

To illustrate the phenomena associated with breaking all symmetries, it is helpful to consider the changes in dynamics seen along a one-dimensional path such as that shown as the dotted line in figure 4. We first chose a value of  $\epsilon_1$  below the thresholds for persistent switching in  $x_2$  and  $x_3$ . For instance, fixing  $\epsilon_1 = 0.0001$  and  $\epsilon_3 = 0.001$  and allowing  $\epsilon_2$  to vary, we see the following types of dynamics.

For the values of the coefficients given above, the choice  $\epsilon_2 = 0.00003$  is a point lying to the right of the homoclinic wedge and to left of the heteroclinic wedge in the first quadrant of figure 4. For these  $\epsilon_2$  and  $\epsilon_3$  values but for  $\epsilon_1 = 0$ , there exists an attracting quasiperiodic solution with  $x_2$  and  $x_3$  both positive. With  $\epsilon_1 = 0.0001$  the same type of quasiperiodic solution exists. As  $\epsilon_2$  is decreased while  $\epsilon_1$  is fixed at 0.0001 we find, as expected, intervals of  $\epsilon_2$  in which there are quasiperiodic attractors interspersed with intervals on which there is locking of the two frequencies associated with the quasiperiodic solution (periodic orbits). In some intervals, period doubling cascades are observed, as is normal near quasiperiodic behaviour. The interchange between locking and quasiperiodic behaviour persists until we approach the homoclinic

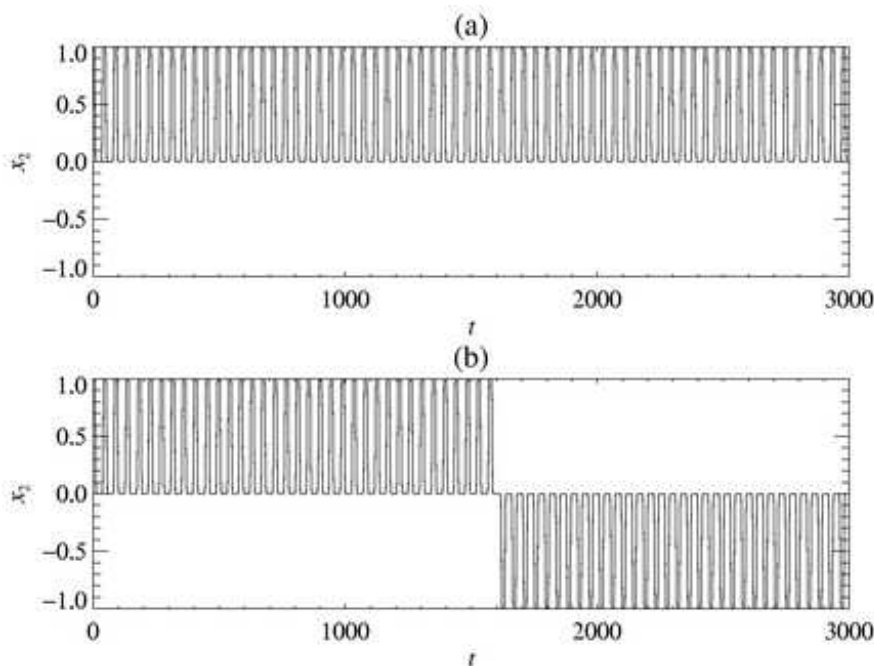


Figure 7. Onset of switching in  $x_2$  for equations (20–22), associated with crossing into the wedge of homoclinic bifurcations of  $P$  in the second quadrant of  $(\epsilon_2, \epsilon_3)$ -space. Parameters  $\epsilon_1 = 0.0001$ ,  $\epsilon_3 = 0.001$  are fixed and  $\epsilon_2$  is decreased: (a)  $\epsilon_2 = -0.000000567$  gives a chaotic attractor confined to the region  $x_2 > 0$ ; (b)  $\epsilon_2 = -0.000000568$  gives a chaotic transient with  $x_2 > 0$ , then the sign of  $x_2$  changes and the orbit is attracted to a quasiperiodic solution with  $x_2 < 0$ . Other coefficients as described in text. Note that the chaotic nature of the orbit in (a) and the transient in (b) is not apparent on the timescale used to plot the time series.

wedge at negative values of  $\epsilon_2$ .

As this homoclinic wedge is approached, apparently chaotic dynamics is observed, consistent with the appearance of horseshoes associated with the impending homoclinic tangency. Before the first tangency is reached, orbits are trapped in the region with  $x_2 > 0$ ,  $x_3 > 0$  (figure 7a). If  $\epsilon_2$  is decreased past the tangency value, the attractor crosses  $W^s(P)$  and so a typical orbit will display a chaotic transient with  $x_2 > 0$ ,  $x_3 > 0$ , and then switch to  $x_2 < 0$ ,  $x_3 > 0$ , after which the orbit is attracted to a quasiperiodic solution in that quarter of phase space (figure 7b). The corresponding Poincaré maps (on the section  $H_1^{\text{in}}$ ) are shown in figure 8. With negative values of  $\epsilon_2$ , once the trajectory has switched to  $x_2 < 0$ , the behaviour is analogous to that observed with  $\epsilon_2 > 0$  and  $x_2 > 0$ : quasiperiodic attractors interspersed with frequency locking. Note there is no persistent switching in  $x_2$ , and no switching in  $x_3$ ,

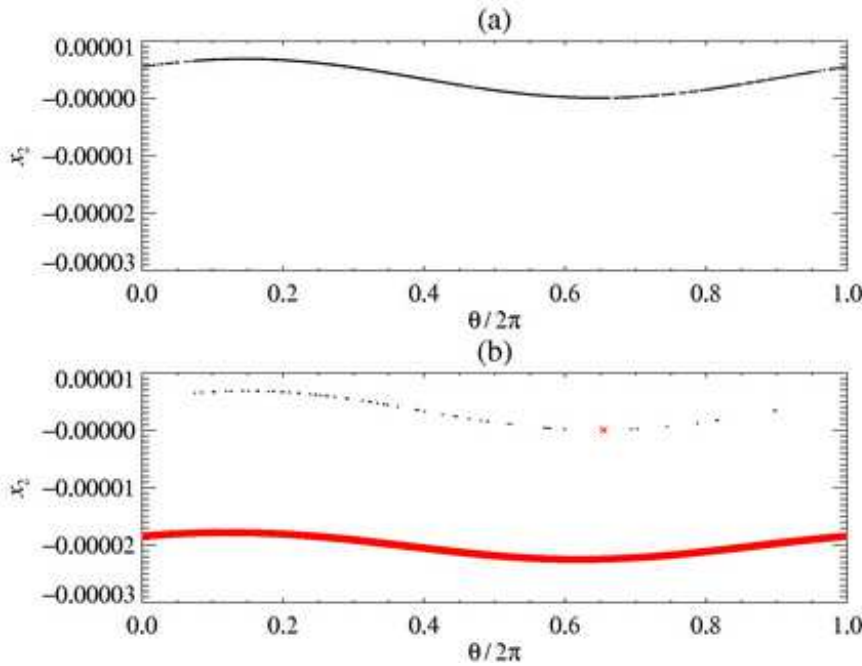


Figure 8. (a) Poincaré map for the orbit shown in figure 7(a); (b) Poincaré map for the orbit in figure 7(b). In each case the Poincaré section is  $H_1^{\text{in}}$  with  $|x_3| = h = 0.005$ . In each panel, a dot (resp. cross) indicates that the orbit next crosses the Poincaré section with  $x_2 > 0$  (resp.  $x_2 < 0$ ).

In (b), the upper collection of dots corresponds to the chaotic transient, which ends in a single cross, after which the orbit switches to a quasiperiodic attractor, represented by the lower collection of crosses.

for these parameter values.

If  $\epsilon_2$  is now increased from  $\epsilon_2 = 0.00003$  while  $\epsilon_1$  and  $\epsilon_3$  are kept fixed as before, we approach the wedge of heteroclinic connections from  $-E_3$  to  $E_2$  (following the dotted line in figure 4). Once the left edge of the heteroclinic wedge has been crossed, orbits can switch from  $x_3 < 0$  to  $x_3 > 0$  (but not from  $x_3 > 0$  to  $x_3 < 0$ ). For example, at  $\epsilon_2 = 0.00011$ , we find a chaotic transient with  $x_3 < 0$  that has a single switch to a locked periodic orbit with  $x_3 > 0$ , in a manner similar to the single  $x_2$  switch in figure 7(b). For larger  $\epsilon_2$ , we find other examples of quasiperiodicity, locked periodic orbits, chaos, chaotic transients and single switches from  $x_3 < 0$  to  $x_3 > 0$ , consistent with the analysis presented above. We did not find any examples of persistent switching.

The behaviour for negative values of  $\epsilon_2$  and/or  $\epsilon_3$  is analogous: single switches can be found, but there is no persistent switching for  $\epsilon_1 = 0.0001$ .

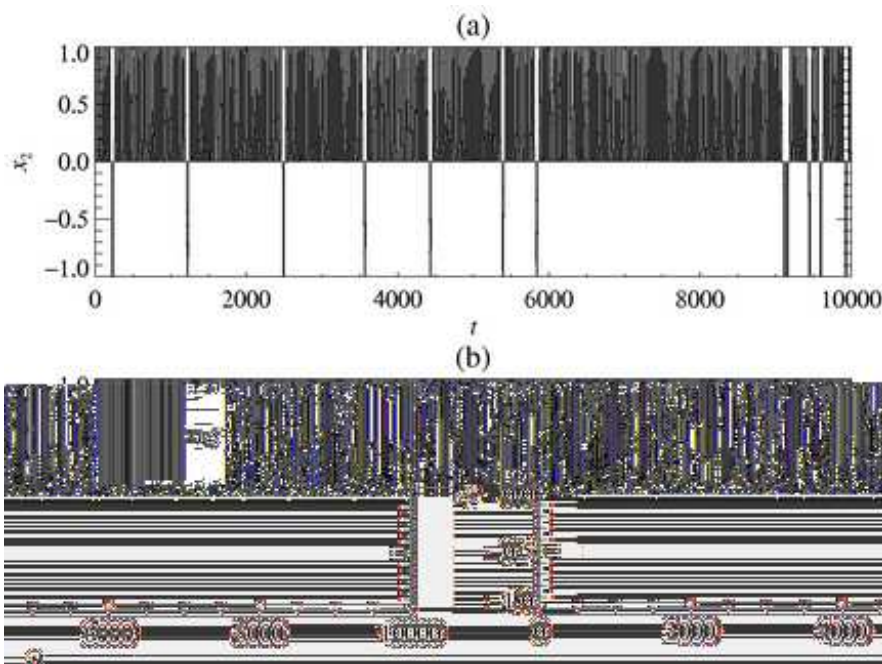


Figure 9. Time series showing persistent switching in  $x_2$  alone, for equations (20–22) with  $\epsilon_1 = 0.0003$ ,  $\epsilon_2 = 0.0002$ ,  $\epsilon_3 = 0.001$ . The other coefficients are as defined in text.

However, persistent switching in one or both of  $x_2$  and  $x_3$  is observed if we increase  $\epsilon_1$ . For our choice of parameters, we can find persistent switching in  $x_2$  only at  $\epsilon_1 = 0.0003$ , and persistent switching in both  $x_2$  and  $x_3$  at  $\epsilon_1 = 0.005$ . We have not tried to find precise values of the thresholds for switching, but note that the threshold for persistent switching in  $x_2$  is lower than that for  $x_3$  for the particular coefficients we use in the differential equations, consistent with our choice of  $d_{23} > d_{33}$ .

Figures 9 and 10 show an example of persistent switching in  $x_2$  (but not  $x_3$ ) for  $\epsilon_1 = 0.0003$ ,  $\epsilon_2 = 0.0002$  and  $\epsilon_3 = 0.001$ . The trajectory crosses the Poincaré section  $H_1^{\text{in}}$  in a curve that appears reasonably smooth at the largest scale (figure 10), but the magnified inset shows that the curve has structure, and that parts of the curve lie below  $W^s(E_2)$ , leading to switches from  $x_2 > 0$  to  $x_2 < 0$ . For these parameter values ( $\epsilon_2 > 0$ ), there appears to be no attractor with  $x_2 < 0$ , so after a short transient, the trajectory switches back to  $x_2 > 0$ .

Dynamics with a larger value of  $\epsilon_1 = 0.005$  are shown in figures 11 and 12: here we have persistent switching in  $x_2$  and  $x_3$ . In the Poincaré section in

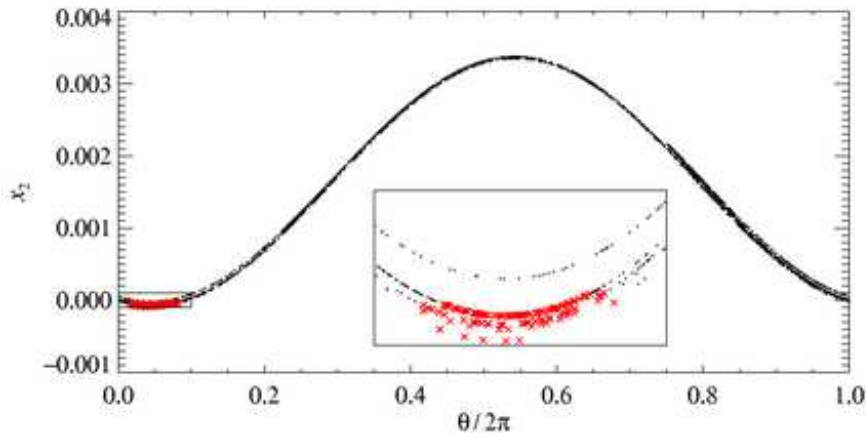


Figure 10. Poincaré section corresponding to the time series shown in figure 9. The inset shows an enlargement of the region in the box marked in the main picture. The Poincaré section is  $H_1^{\text{in}}$  with  $|x_3| = h = 0.01$ . A dot (resp. cross) indicates that the orbit next crosses the Poincaré section with  $x_2 > 0$  (resp.  $x_2 < 0$ ). The inset shows that crosses (indicating a switch) occur where the trajectory lies below  $W^s(E_2)$ .

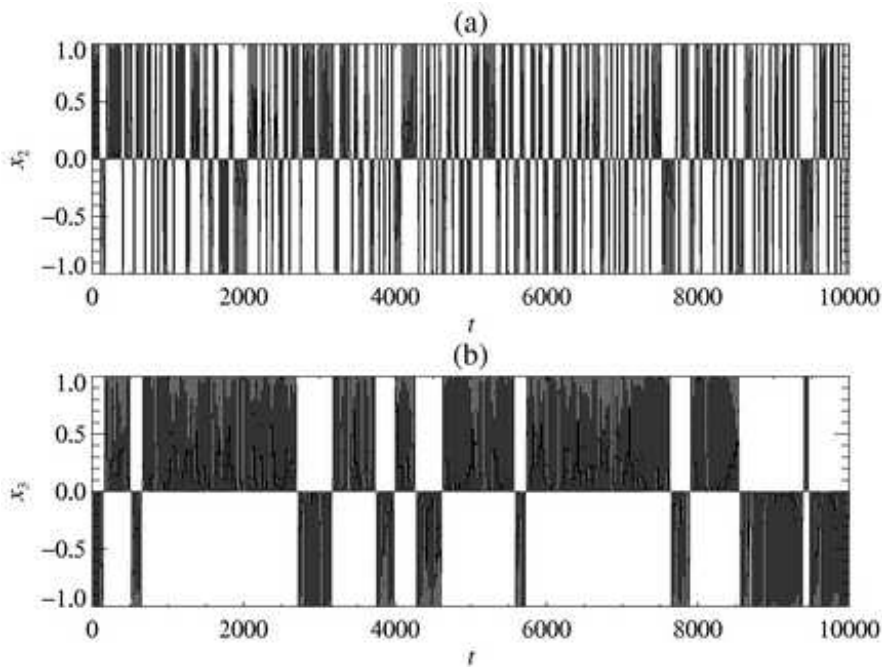


Figure 11. Time series showing persistent switching in  $x_2$  and  $x_3$ , for (20–22) with  $\epsilon_1 = 0.005$ ,  $\epsilon_2 = 0.00003$ ,  $\epsilon_3 = 0.001$ . Other coefficients as defined in text.

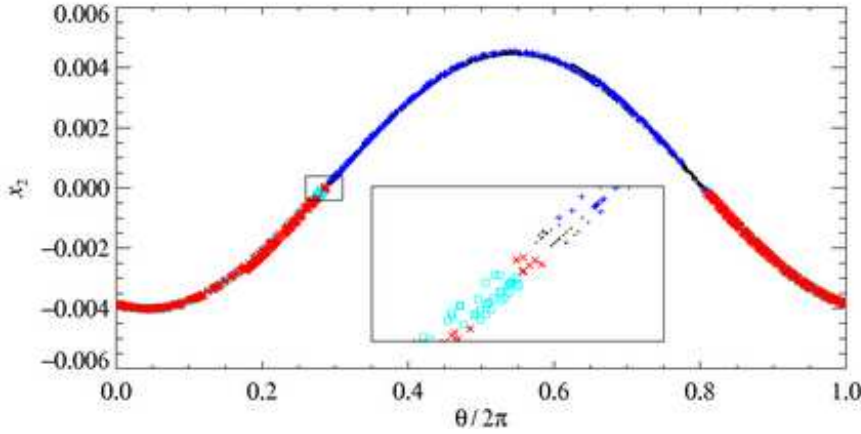


Figure 12. Poincaré section corresponding to the time series shown in figure 11. The inset shows an enlargement of the region in the box marked in the main picture. The Poincaré section is  $H_1^{\text{in}}$  with  $|x_3| = h = 0.01$ . Four symbols are used: a dot (resp. cross) indicates that the orbit next crosses the Poincaré section with  $x_2 > 0$  (resp.  $x_2 < 0$ ) and with  $x_3 > 0$ . A + (resp. square) indicates that the orbit next crosses the Poincaré section with  $x_2 > 0$  (resp.  $x_2 < 0$ ) and with  $x_3 < 0$ . The division between orbits falling either side of  $W^s(E_2)$  is clearly visible. Orbits falling on opposite sides of  $W^s(E_3)$  are reasonably well mixed with this choice of cross-section.

figure 12, we use four symbols to indicate the future trajectory of the orbit around the cycle: a dot, cross, plus or square indicates that the trajectory will visit the  $(x_2 > 0, x_3 > 0)$ ,  $(x_2 < 0, x_3 > 0)$ ,  $(x_2 > 0, x_3 < 0)$  or  $(x_2 < 0, x_3 < 0)$  quadrant before returning to  $H_1^{\text{in}}$ . The inset shows that dot and plus ( $x_2 > 0$ ) are well separated from cross and square ( $x_2 < 0$ ), which is not surprising since it is at the section  $H_1^{\text{in}}$  that the trajectory decides between  $+E_2$  and  $-E_2$ . In contrast, the future choice between  $+E_3$  and  $-E_3$  can be seen to be reasonably well mixed.

Our understanding of the mechanism behind persistent switching in  $x_2$  or  $x_3$  requires that  $\epsilon_1$  be large enough that  $1 + \epsilon_1 g_3(\theta)$  or  $1 + \epsilon_1 g_1(\theta)$  can take on positive and negative values, as a function of  $\theta$ . In order to illustrate this effect, we have fitted these functions using the trajectories in figures 9 ( $\epsilon_1 = 0.0003$ ) and 11 ( $\epsilon_1 = 0.005$ ). We have concentrated on switching in  $x_3$ , so the fact that these trajectories are for different values of  $\epsilon_2$  does not affect our conclusions. We took the coordinates  $(x_3, \theta_1)$  on the section  $H_1^{\text{out}}$  and  $\tilde{x}_3$  from the next intersection with  $H_2^{\text{in}}$ , and used these data to fit a map of the form of  $\Psi_{12}$ :

$$\tilde{x}_3 = x_3 (A_1 + \epsilon_1 f_1(\theta_1)) + \epsilon_3 (1 + \epsilon_1 g_1(\theta_1)),$$



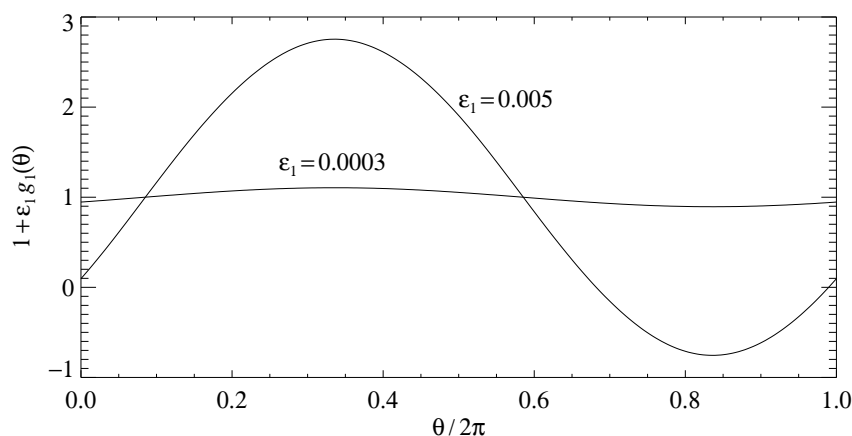


Figure 13. The function  $1 + \epsilon_1 g_1(\theta)$  fitted to the data in figures 9 ( $\epsilon_1 = 0.0003$ ) and 11 ( $\epsilon_1 = 0.005$ ). This function must be both positive and negative as a function of  $\theta$  in order to allow persistent switching in  $x_3$ .

see equation (6). We represented the two functions  $f_1$  and  $g_1$  by a finite Fourier series, and were able to fit the data to within one part in 1000 for all points with the smaller value of  $\epsilon_1$ , and to within one part in 100 for all but a handful of the points for the larger value of  $\epsilon_1$ . As expected, the  $A_1 + \epsilon_1 f_1$  part of the map remains positive, but  $1 + \epsilon_1 g_1$  can change sign for the larger value of  $\epsilon_1$ , as shown in figure 13. Indeed, the numerical ratio of the amplitudes of the two fitted functions is 16.663 while the ratio of the two values of  $\epsilon_1$  is 16.667. Our understanding requires the change in sign of  $1 + \epsilon_1 g_1$  as a necessary condition for persistent switching in  $x_3$ , which is confirmed by this illustration and by our other calculations. A similar transition occurs (at a smaller value of  $\epsilon_1$ ) at the onset of persistent switching in  $x_2$ , and in that case, the data can be fitted to within 1 part in 10,000 or better.

We note that we were able to find parameter values associated with persistent switching in  $x_2$  alone but were unable to get persistent switching in  $x_3$  without also having switching in  $x_2$ . This is a consequence of the particular choice of symmetry-breaking coefficients we use: the threshold in  $\epsilon_1$  for persistent switching in  $x_3$  is higher than the threshold for persistent switching in  $x_2$  for the chosen coefficients. For other parameters, the thresholds would be the other way around.

In the numerical simulations described above, the quantities  $\delta_1$ ,  $\delta_2$ ,  $\delta_3$  and  $\delta$  were all greater than one; this choice was made to ensure that that the

heteroclinic cycle was attracting in the fully symmetric case and to remove any possible complications due to chaotic dynamics associated with homoclinic bifurcations of  $\pm E_2$  and  $\pm E_3$ . Much of the same switching dynamics should still occur if one or both of  $\delta_2$  and  $\delta_3$  is less than one while  $\delta > 1$ , but in that case there may be additional complications in the dynamics associated with the homoclinic bifurcations of the equilibria.

## 6 Conclusions

This paper has investigated the effect of small symmetry-breaking on the dynamics near a structurally stable heteroclinic cycle connecting two equilibria and a periodic orbit. The heteroclinic cycle is structurally stable in the case that there are two reflection symmetries and a rotation symmetry in the underlying system; we were interested in the dynamics seen when one or more of the symmetries is broken. It was reported in [19] that this type of system can exhibit seemingly chaotic dynamics along with repeated but irregular switching of sign of various variables, but details of the mechanisms underlying the onset of complicated dynamics were not explored there. In this paper, we have identified global bifurcations that induce the onset of chaotic dynamics and switching near a heteroclinic cycle of this type. These turn out to be homoclinic tangencies between the stable and unstable manifolds of the periodic orbit, and specific heteroclinic tangencies between stable and unstable manifolds of the two equilibria. By construction and analysis of approximate return maps, we were able to (approximately) locate the global bifurcations in parameter space and hence to isolate instances of the different types of switching and chaotic dynamics in a specific numerical example.

In addition to identification of the mechanisms underlying the onset of switching, two important insights have been gained from this study. First, we found that interaction of the different symmetry-breaking terms is required for switching; partial symmetry breaking (where one or two of the three symmetries are retained) did not result in switching. Switching results from the right combination of a global bifurcation (which results in turn from breaking of the rotation symmetry) and small breaking of at least one of the reflection symmetries. Second, we found there is a threshold in  $\epsilon_1$  below which there can be single switches in the signs of certain variables but no persistent switching.

The important point here is that persistent switching does not result from arbitrarily small symmetry breaking, but is a ‘large’ symmetry-breaking effect. Of course, as usual ‘small’ and ‘large’ are relative terms, and addition of seemingly tiny symmetry-breaking effects might actually result in persistent switching, as was the case in the numerical example we investigated in section 5.

One aspect of this problem which has not yet been investigated is whether it is possible to make *a priori* predictions about switching rates or derive scaling laws for switching times. It seems plausible that switching rates and times might depend on the ‘distance’ from the global bifurcation that induces the switching, but no detailed attempts have yet been made to quantify such a relationship. The statistics of switching intervals were measured in the related model of [19], who report an exponential distribution of intervals between switches.

Finally, we note that the dynamo model studied in [19] has a symmetry that is never broken (this is the symmetry  $(z_1, x_2, x_3) \rightarrow (-z_1, -x_2, -x_3)$  in the notation of that paper). Retention of this symmetry while breaking all others amounts to retaining invariance of the  $z_1 = x_2 = x_3 = 0$  subspace, and will also have to consequence of relating the dynamics in different parts of the phase space. For example, if it is possible to switch from  $(x_2 > 0, x_3 > 0)$  to  $(x_2 > 0, x_3 < 0)$ , it will also be possible to switch from  $(x_2 < 0, x_3 < 0)$  to  $(x_2 < 0, x_3 > 0)$ . Our results do not include this effect, and retaining this symmetry may well have profound effects on the switching properties. Nevertheless we expect our basic ideas about switching being induced by a balance between a global bifurcation and symmetry-breaking terms and the existence of a threshold for persistent switching to apply quite generally, and to the example in [19] in particular, even if the details turn out not to be directly relevant.

## Acknowledgments

We thank Ian Melbourne, Edgar Knobloch and Jeff Porter for helpful conversations. This research has been supported by grants from New Zealand Institute for Mathematics and its Applications, University of Auckland Research Council, London Mathematical Society and EPSRC.

## References

- [1] Field, M., 1980, Equivariant dynamical systems. *Trans. Am. Math. Soc.*, **259**, 185–205.
- [2] Guckenheimer, J. and Holmes, P., 1988, Structurally stable heteroclinic cycles. *Math. Proc. Camb. Phil. Soc.*, **103**, 189–192.
- [3] Melbourne, I., 1991, An example of a non-asymptotically stable attractor. *Nonlinearity*, **4**, 835–844.
- [4] Krupa, M. and Melbourne, I., 1995, Asymptotic stability of heteroclinic cycles in systems with symmetry. *Ergod. Th. & Dynam. Sys.*, **15**, 121–147.
- [5] Krupa, M. and Melbourne, I., 2004, Asymptotic stability of heteroclinic cycles in systems with symmetry, II. *Proc. Roy. Soc. Edinburgh A*, **134**, 1177–1197.
- [6] Kirk, V. and Silber, M., 1994, A competition between heteroclinic cycles. *Nonlinearity*, **7**, 1605–1621.
- [7] Ashwin, P. and Chossat, P., 1998, Attractors for robust heteroclinic cycles with continua of connections. *J. Nonlinear Sci.*, **8**, 103–129.
- [8] Aguiar, M., Castro, S. and Labouriau, I., 2005, Dynamics near a heteroclinic network. *Nonlinearity*, **18**, 391–414.
- [9] Postlethwaite, C.M. and Dawes, J.H.P., 2005, Regular and irregular cycling near a heteroclinic network. *Nonlinearity*, **18**, 1477–1509.
- [10] Scheel, A. and Chossat, P., 1992, Bifurcation d’orbites périodiques à partir d’un cycle homoclinic symétrique. *C. R. Acad. Sci. Paris*, **341**, 49–54.
- [11] Chossat, P., Krupa, M., Melbourne, I. and Scheel, A., 1997, Transverse bifurcations of heteroclinic cycles in symmetric systems. *Physica D*, **100**, 85–100.
- [12] Postlethwaite, C.M. and Dawes, J.H.P., 2006, A codimension two resonant bifurcation from a heteroclinic cycle with complex eigenvalues. *Dyn. Syst. Int. J.* in press.
- [13] Busse, F.H. and Heikes, K.E., 1980, Convection in a rotating layer – simple case of turbulence. *Science*, **208**, 173–175, 1980.
- [14] Proctor, M.R.E. and Jones, C.A., 1988, The interaction of two spatially resonant patterns in thermal convection. I. Exact 1:2 resonance. *J. Fluid Mech.*, **188**, 301–335.
- [15] Armbruster, D., Guckenheimer, J., Holmes, P., 1988, Heteroclinic cycles and modulated traveling waves in systems with  $O(2)$  symmetry. *Physica D*, **29**, 257–282.
- [16] Melbourne, I., 1989, Intermittency as a codimension three phenomenon *J. Dyn. Stab. Sys.*, **1**, 347–367.
- [17] Chossat, P., 1993, Forced reflectional symmetry breaking of an  $O(2)$ -symmetric homoclinic cycle. *Nonlinearity*, **6**, 723–731.
- [18] Sandstede, B. and Scheel, A., 1995, Forced symmetry breaking of homoclinic cycles. *Nonlinearity*, **8**, 333–365.
- [19] Melbourne, I., Proctor, M.R.E. and Rucklidge, A.M., 2001, A heteroclinic model of geodynamo reversals and excursions. In: P. Chossat, D. Armbruster and I. Oprea (Eds) *Dynamo and Dynamics, a Mathematical Challenge* (Dordrecht: Kluwer), pp. 363–370.
- [20] Stone, E. and Holmes, P., 1990, Random perturbations of heteroclinic attractors. *SIAM J. Appl. Math.*, **50**, 726–743.
- [21] Armbruster, D., Stone, E., Kirk, V., 2003, Noisy heteroclinic networks. *Chaos*, **13**, 71–79.
- [22] Clune, T. and Knobloch, E., 1994, Pattern selection in three-dimensional magnetoconvection. *Physica D*, **74**, 151–176.
- [23] Kirk, V., Lane, E., Silber, M., 2006, A mechanism for switching in a heteroclinic network. In preparation.
- [24] Ashwin, P., Rucklidge, A.M. and Sturman, R., 2004, Two-state intermittency near a symmetric interaction of saddle-node and Hopf bifurcations: a case study from dynamo theory. *Physica D*, **194**, 30–48.
- [25] Rucklidge, A.M. and Matthews, P.C., 1995, The shearing instability in magnetoconvection. In:

- A. Brandt and H.J.S. Fernando (Eds) *Double-Diffusive Convection* (Washington: American Geophysical Union), pp. 171–184.
- [26] Matthews, P.C., Rucklidge, A.M., Weiss, N.O. and Proctor, M.R.E., 1996, The three-dimensional development of the shearing instability of convection. *Phys. Fluids*, **8**, 1350–1352.
  - [27] Rucklidge, A.M., 2001, Global bifurcations in the Takens–Bogdanov normal form with  $D_4$  symmetry near the  $O(2)$  limit. *Phys Lett A*, **284**, 99–111.
  - [28] Ashwin, P., Field, M., Rucklidge, A.M. and Sturman, R., 2003, Phase resetting effects for robust cycles between chaotic sets. *Chaos*, **13**, 973–981.
  - [29] Ashwin, P., Rucklidge, A.M. and Sturman, R., 2004, Cycling chaotic attractors in two models for dynamics with invariant subspaces. *Chaos*, **14**, 571–582.
  - [30] Glendinning, P. and Sparrow, C., 1984, Local and global behaviour near homoclinic orbits *J. Stat. Phys.*, **35**, 645–696.
  - [31] Guckenheimer, J. and Holmes, P., 1986, *Nonlinear Oscillations, Dynamical Systems, and Bifurcations of Vector Fields* (second edition). Springer-Verlag, New York.
  - [32] Press, W.H., Flannery, B.P., Teukolsky, S.A. and Vetterling, W.T., 1986, *Numerical Recipes – the Art of Scientific Computing*. Cambridge University Press, Cambridge.
  - [33] Parker, T.S. and Chua, L.O., 1989, *Practical Numerical Algorithms for Chaotic Systems*. Springer, New York.